Tampere University

Oloruntobiloba Kolawole

ASTEROID ANALOGUE DESIGN FOR RADAR TOMOGRAPHY

Mathematical Model, Data Analysis and 3D-Printed Objects

Master of Science thesis
Faculty of Information Technology and Communication Sciences (ITC)
Examiners: Prof. Sampsa Pursiainen
Doctoral Student Yusuf Oluwatoki Yusuf
December 2022

Abstract

Oloruntobiloba Kolawole: ASTEROID ANALOGUE DESIGN FOR RADAR TOMOGRAPHY
Mathematical Model, Data Analysis and 3D-Printed Objects
Master of Science Thesis
Tampere University
Master's Degree Programme in Computing Sciences
Supervisor: Professor Sampsa Pursiainen
The Dean of the Faculty of Information Technology and Communication Sciences approved the topic and supervisor on 8th June 2022.

Technology and complexity in space exploration have significantly enhanced, much like in other fields. Improved space missions through data analysis and lab simulations are continually adding to the richness of knowledge and the enormous database of space objects. The overarching theme of this thesis was to create an analogue with a predetermined permittivity structure that may be utilized using computational methods to find fractures inside the complex 3D model of the asteroid Itokawa.

We focused on creating a wireframe that can be 3D printed by replacing a tetrahedral mesh's edges with overlapping prisms. We numerically validated the Wireframe Function's functionality by analysing the measured error, loss tangent, and imaginary as well as real permittivities of the model using Matlab and other scientific tools. Several test objects were printed using the Original Prusa i3 MK3S+ printer before the final 3D model was printed to guarantee the model's functionality.

The findings showed that the ideal permittivity of a complex asteroid model could be controlled and thus 3D printed using specific settings and materials such as the ABS450 to show varying layers, edges, and fractures due to the model's edge width and volumetric filling relationship. The findings also showed that when both edge threshold and correction were applied, we obtained the optimal result that was closest to the referential data.

Keywords: Numerical Analysis, Computer Radar Tomography (CRT), Signal Processing, Asteroids, Permittivity, Edge Threshold, Correction, 3D Printing.

As I grow older, I appreciate more the man you were, so this thesis is dedicated to my late father, Professor Joseph Kolawole. Thank you for imparting so much wisdom through your words and deeds. You will live on in our hearts forever.

Acknowledgements

I want to thank God first and foremost because, without Him, none of this would have been possible. I also want to express my sincere gratitude to my supervisor, Professor Sampsa Pursiainen, for his constant advice, support, and time invested in making this body of work a reality. I appreciate his enthusiasm and insightful criticism, which significantly improved this work. I also like to thank the Academy of Finland (ICT2023 Project, FETD-Based Tomographic Full-Wave Radar Imaging of Small Solar System Body Interiors, number 336151) for funding this thesis. Tampere University has also given me a full scholarship for my master's program's entire duration and for that I am grateful. Thanks to all my classmates and professors in Tampere University's data science program, it has been a pleasure to interact with so many brilliant minds. I thank my senior colleagues Yusuf Oluwatoki Yusuf and Fernando Galaz Prieto for their technical input and advice. I want to thank Mika Kiirikki from TUNI's FABLAB for his thoughtful input on 3D printing. I will also like to thank Vincent Laur and Jean-Michel Geffrin for permission granted to use their respective lab measurements. Last but not least, I would not have been able to complete this thesis without the support and love of my family and friends. I sincerely appreciate my mother, Associate Professor Susan Kolawole, and my siblings, Oluwabukola Olaniyan, Dr Babatunde Kolawole, Dr Oluwatayo Kolawole, Oluwabunmi Adeojo as well as each of their families. Your prayers, love, and support enabled me to complete my masters education. My friends Oluwanifise Adeleke, Precious Okwaraebuzie, and Shehani Athalage have prayed for me, given me words of encouragement, and supported me, I value our friendship. I would like to thank Bolarinwa and Olayinka Akindaini as well as Sarastus and Miimu Hietanen for opening up their respective homes to me, I truly appreciate the hospitality. To Onosedeba Eichie, thank you for your unwavering support and sacrifices throughout the master's program; your love, kind spirit and prayers are priceless to me.

Contents

List of Figures

List of Tables

ABBREVIATIONS AND SYMBOLS

3D: Three-dimensional.

ESA: European Space Agency.

JAXA: Japan Aerospace Exploration Agency.

NASA: National Aeronautics and Space Administration.

Osiris-REx: Origins Spectral Interpretation Resource Identification Security Regolith Explorer.

SSSB: Small Solar System Body.

CRT: Computed Radar Tomography.

5G: Fifth Generation.

6G: Sixth Generation.

CUBESATs: A group of spacecraft for research purposes known as Nanosatellites.

NEA: Near Earth Asteroid.

DART: Double Asteroid Redirection Test.

DRACO: Didymos Reconnaissance and Asteroid Camera for Optical navigation.

ABS: Acrylonitrile Butadiene Styrene

PLA: Polylactic Acid

1 Introduction

1.1 Overview

Asteroids hit the earth now and then (Talbert 2021; Reich 2010). Although asteroids large enough to cause significant destruction to the earth and its inhabitants are quite unusual, it would be quite catastrophic if an asteroid large enough to cause such damage entered the earth's orbit and was headed directly to the earth. Hence, an understanding of asteroids, their physical and chemical properties as well their internal composition by leveraging data, mathematical modelling and modern technology cannot be overemphasised as this would aid scientists and relevant authorities in creating sturdy models for planetary defence and space mining.

In the 1900s only a few hundred near-earth asteroids had been discovered, however, as of mid-2021, NASA recorded approximately twenty-six thousand near-earth asteroids, 2000 of them posing an imminent threat to the earth (Bottke et al. 2015; Erasmus et al. 2017). This is a testament to the giant technological leaps that have occurred in recent years bringing about so many opportunities and developments in different spheres of life, including but not limited to space. Hence scientists are no longer stifled by the unavailability of data as well as an inability to effectively monitor, analyse and forecast the behaviours of small solar system bodies (SSSBs) due to computational power but are rather able to model and simulate SSSBs, their internal and external properties, landing areas (Wang et al. 2020), surfaces as well as the internal composition (Sorsa et al. 2019) of these bodies for further analysis.

Furthermore, collaborative efforts between NASA and ESA have brought about the mission for Asteroid Impact & Deflection Assessment (AIDA) whose aim is to analyze mission elements from NASA's ongoing DART mission (Double Asteroid Redirection Test) which is targeted at the binary asteroid system 65803 Didymos as well as to measure the deflection outcome from ESA's upcoming mission HERA which will rendezvous and characterise the same target in 2027 (Cheng et al. 2018). This is just one of the many research efforts that have been made and are still being made by various scientists and concerned authorities to understand extensively the individual properties of SSSBs. However, for missions such as this to be very efficient, scientists must have a clear understanding of every scenario that can or may play out while in a time-bound space mission. Hence, it is beneficial for simulations about these missions to be carried out prior to the

actual mission time.

Moreover, advancements in material technology have brought about the possibility of controlling the volume fraction and permittivity ratio when creating 3D complex structured objects (Sorsa et al. 2021b). The research efforts in (Pursiainen and Kaasalainen 2016) as well as in (Sorsa et al. 2019) have also brought a deeper understanding of the internal properties (dielectric properties and void deep spaces) of the asteroid Itokawa. By extending the research carried out in Sorsa et al. 2019, this thesis will study creating a complex asteroid analogue model for tomographic radar measurements and present an advanced approach to determine the ideal permittivity ratios of the model asteroid Itokawa (JAXA 2003; Fujiwara et al. 2006).

1.1.1 Statement of Problem

Small solar system bodies such as asteroids and comets are part of the numerous objects that make up the solar system. Just like the human brain, we are aware of the existence of these bodies but do not fully understand their properties or entire capabilities. Additionally, because of the cost of space exploration missions, it will be quite cumbersome and very expensive to frequently carry out physical analysis on small solar system bodies, it is rather more realistic and cost-effective to create 3D asteroid models with the same properties as the real asteroids for further analysis. In view of this, the intention of this study is to provide solutions to the following problems:

1. The lack of in-depth knowledge about the interior properties of the asteroid Itokawa.

2. The unavailability of a 3D modelled asteroid with ideal properties as the measurements taken from the Itokawa (JAXA 2003; Fujiwara et al. 2006) asteroid regolith by the Japanese Aerospace Exploration Agency (JAXA).

1.1.2 AIM

This study aims to prepare a model for printing 3D analogous structures of small solar system bodies specifically the asteroid Itokawa using computational methods. This will enable scientists to have a better understanding of the internal structures and properties of small solar system bodies. It will also help to determine the ideal parameters such as the permittivity ratio, the edge threshold and internal fractures that fit the 3D model which is most in line with the physical, geological, and chemical properties of the asteroid Itokawa. In summary, the aim of this study is to:

1. To develop an analogue with a preset permittivity structure that can be used to locate

fractures inside the intricate 3D model of the asteroid Itokawa using lab measurements and computational techniques. (Fujiwara et al. 2006).

2. Determine the ideal edge threshold and printer resolution for printing complex 3D asteroid models.

3. Present a tool to construct a wireframe from a finite element mesh with a given permittivity structure.

2 Literature Review

In recent years, the advancements in technology have been immense, giving birth to a vast array of opportunities, especially with the rise of artificial intelligence, data science, the 5G & 6G technologies as well as advancements in space technologies including but not limited to satellites, spacecraft, space stations. In 2021, the technology giant, Facebook announced that its company would change its name to 'Meta' (Times 2021) and will be more focused on the metaverse which utilises recent technologies to create a 3D virtual reality of human interaction at record-breaking speeds (Dionisio et al. 2013). However, such high-powered technology which is modelled on the Universe will not have been possible without an understanding of man's interaction on the earth, the earth's interaction with other space objects as well as the solar system in general. This is a testament to the importance of space exploration as its significance not only lies with space mining and planetary defence but also in various technologies as seen with Meta. Hence scientists must continue to dive deeper into research about space to understand deeply the properties and capabilities of space objects.

2.1 Evolution of the Solar System

The Universe is made up of innumerable galaxies, with the Milky Way Galaxy which comprises our solar system, being just one of the many. There have been various accounts as to how this solar system originated, while some believe that it was formed through an interstellar cloud and an accumulation of matter around the sun (Alfvén 1982) others believed that it was formed from a collision of dust and comic gases (O'Leary 1999). One common element to various accounts is that the solar system is approximately five billion years old and comprises the sun, stars, planets, asteroids, comets and solar bodies.

For decades, scientists believed that the solar system was comprised of nine planets. However, in the past sixty to seventy years there have been tremendous discoveries about the number of objects in the solar system, as well as the composition and properties of these objects (Persico et al. 2018). In 2006, the International Astronomical Union (IAU) responsible for the safeguarding of high-powered astronomy agreed that Pluto did not meet all the requirements to be labelled a planet and downgraded it to a dwarf planet (McDaid 2006). In addition, recent studies have shown that there are about double the number of asteroids that are embedded in the asteroid belt as previously believed to exist. As science continues to evolve and new technologies constantly

emerge, more discoveries have been and will continue to be made about the number of objects in our solar system, their properties as well as their composition. Consequently, these eight planets are divided into two categories; namely the terrestrial planets and the Jovian Planets.

2.1.1 Terrestrial Planets

The terrestrial planets, which include Mars, Venus, Mercury, and Earth, are the planets closest to the sun and are classified as such due to their composition. Generally, terrestrial planets have a rocky and compact surface and do not have rings (NASA 2022b).

2.1.2 Jovian Planets

The Jovian Planets, also known as the outer planets; Saturn, Neptune, Jupiter, and Uranus are classified under this category also mainly because of their composition. Unlike the terrestrial planets, they do not have solid surfaces but are rather composed of various elements and gases such as hydrogen, helium and ammonia (NASA 2022b). These planets have rings and are relatively larger in comparison to terrestrial planets.

2.1.3 Small Solar System Bodies

Small Solar System Bodies also referred to as SSSBs, are a classification of solar system bodies which consist of asteroids, comets, and small planetary satellites. These bodies usually have an irregular shape and just like planets, they orbit around the sun.

2.2 Planetary Science

Planetary Science is the study of the characteristics and origin of planets and their planetary systems, the interaction between these planets and systems as well as the evolution of these planets and systems (Jones 2022). Research in space exploration is one of the oldest branches in astronomy (O'Leary 1999). While this research has been ongoing for years, early scientists were, however, stifled by a lack of equipment and modern technology. Thus, their contribution to the subject matter was more qualitative. In recent years due to the possibilities brought about by computer simulations and advancements in modern technology, scientists have been able to travel to and from space and assign unmanned vehicles to carry back space samples to the earth.

One major milestone in space exploration was the deployment of the first artificial satellite; Sputnik 1 in October 1957 (Sinelnikov et al. 2014). Since then scientists have continued to explore and study various space objects, thus leading to new discoveries of and about space objects. There

have also been so many more noteworthy milestones in space exploration such as a successful data recovery mission from the planet Venus in December 1962 (Colin 1980), Neil Armstrong walking on the moon in 1969 (West 2022), the launch of a space station in April 1971 (Ivanovich and Ivanovich 2008), the recovery of asteroid samples back to earth by Hayabusa in June 2010 (Fujiwara et al. 2006), the discovery of water on mars (Sorsa 2018), and a successful landing on the far side of the moon in 2019 (Li et al. 2020) to name a few.

Furthermore, the relentless efforts that various space agencies have put into space research are noteworthy as there have been so many breakthrough technologies such as the deployment of CUBESATs, and the use of CTR for examining the interior of space objects, 5G & 6G satellite networks and much more.

2.2.1 Asteroids

Small solar system bodies that are irregularly shaped and have a composition of rocks and minerals are known as asteroids (Sorsa 2018). Just like comets, asteroids are celestial bodies which are the residues of the formation of the solar system billions of years ago. In various regions of the solar system are several objects, such objects include asteroids which can be classified based on location as:

i **Near Earth Asteroids (NEA):** consisting of asteroids whose orbit is close to the earth. Asteroids that can endanger the earth are categorised in this group.

ii **Main Belt Asteroids:** consisting of asteroids whose orbit is between Jupiter and Mars. Approximately 2 million asteroids can be found in the main asteroid belt which are 1 km larger in girth and millions of other asteroids with smaller sizes (Suzy 2022).

iii **Trojan Asteroids:** consisting of asteroids that co-orbit Jupiter (Hestroffer et al. 2019).

Another grouping category for asteroids is based on their shapes, colour, reflective power and surface materials. This classification is divided into three broad categories, namely:

i **C-type Asteroids:** Asteroids with dark carbonaceous objects. The C-type asteroids are quite large in number and make up approximately 75% of known asteroid types.

ii **S-type Asteroids:** Asteroids with stony objects. This group makes up approximately 17% of known asteroid types.

iii **U-type Asteroids:** Asteroids with unknown properties that are neither categorised as C-type or S-type Asteroids.

2.2.2 The Interior Composition of Asteroids

Being one of the least adulterated materials from the inception of the solar system, the interior structures of asteroids are essential to understanding the history and the origin of the solar system (Bottke Jr et al. 2002). Although records of the primary components of the solar Nebula that formed the planets are embedded in the most primitive asteroids (Bottke et al. 2015), what is inside of these asteroids remains an enigma. Although scientists have been asking the question, "What is in the interior of asteroids for years", and there have been relentless research efforts to find out the answer to this question, there have only been a handful of spacecraft to land on an asteroid. However, recent numerical research in tomography reconstructions of a realistic internal distribution model has been able to detect certain deep interior components such as boulders, cracks, voids and details with low contrast in an asteroid model (Sorsa 2021).

2.3 Asteroid Missions

In the last century, there has been ongoing research about various space objects and therefore a number of space missions. Some of these have already been completed such as the Hayabusa 1 & 2, DART, Osiris-Rex and Rosetta missions while some are ongoing and planned for the futures such as the Hera mission.

2.3.1 Completed Missions

Hayabusa 1

In 2005 JAXA initiated the first mission to land on a near-earth asteroid called Itokawa and return sample materials from it using a spacecraft called Hayabusa.

Osiris-REx

In 2018, NASA initiated the Osiris-REx mission to explore the c-type near earth asteroid 101955 Bennu.(Berry et al. 2013) The aim of this mission was to study in detail, return regolith samples, map the global properties of the Bennu asteroid, document the sample site, understand the interaction between the asteroids orbit and its thermal properties as well as compare earth based telescopic observations with the spacecraft observations (Lauretta et al. 2017).

Hayabusa 2

The second Hayabusa mission (Hayabusa 2) organized by JAXA in June 2018 arrived at the asteroid 16173 Ryugu and surveyed the asteroid for approximately 1.5 years. It completed numerous mission

operations such as remote sensing, robot separations and crater formation and returned samples back to earth in 2020 (Kuninaka 2020).

Rosetta

The ROSETTA mission organised as a follow-up mission to the GIOTTO mission in November 1993, was a collaborative mission between ESA and NASA. The ROSETTA lander PHILAE and the ROSETTA orbiter made up the mission elements (Glassmeier et al. 2007).

DART

DART was a space mission that launched in October 2022. Its aim was to use a single spacecraft to impact the near-earth asteroid Didymos and try to change its natural orbital route (Cheng et al. 2012). It used a kinetic impactor as a defence mechanism and Computed Radar Tomography to investigate the asteroid Didymos and its orbit. This mission reinforced the idea that the surface of an asteroid can be compared to a massive pile of rubble (NASA 2022a). Figure 2.1 shows the final images of the asteroid Dimorphos taken before the final impact.

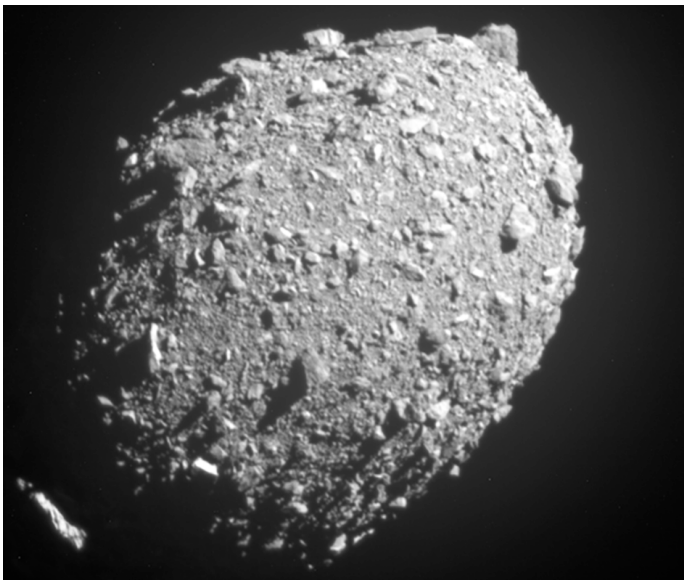

Figure 2.1 *NASA's DRACO spacecraft captured images of the asteroid Dimorphos. It appears to be a massive pile of rubble with inconsistent edges. (NASA 2022a)*

2.3.2 Planned Missions

HERA

HERA is a planned space future mission set to launch in 2024, its aim is to visit three near-earth asteroids and recover samples from these asteroids (Sears et al. 2004). This mission is of great

importance as it plans to implement radar investigations using low-frequency radars (Eyraud et al. 2020).

2.4 Computed Radar Tomography

Radar tomography is a powerful method for obtaining high-resolution images of intricate objects that has gained a lot of popularity recently. It has widespread use in several industries, including geology, engineering, and biotechnology, to carefully analyze an object's internal features (Yusuf et al. 2022). Using radars to visualise and evaluate what is beneath the surface of structures is not a new phenomenon, dating as far back as the 1950's scientists had begun to explore ground penetrating radar (GPR) technology to examine the depth of glaciers and this technology is commonly used today for geological explorations and mining. Airborne ground penetrating radar presented a more advanced technology that proved to be cost-effective and didn't require physical contact with surfaces but performed evaluations using an antenna (Catapano et al. 2011), such technology brought about the possibility of simulating and modelling unknown objects (Jol 2008). Computed Radar Tomography (CRT) is an even more advanced technological approach which builds up on the GPR technology and it applies antennas with multi frequencies to examine larger areas in a shorter time frame.

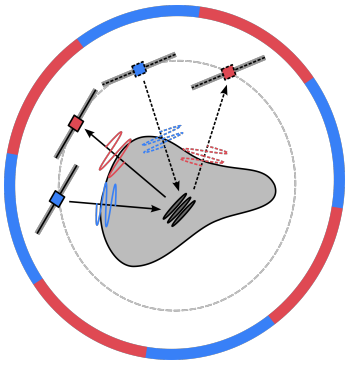

Figure 2.2 *CRT using radio signals to probe the undersurface of an asteroid*

One would think that the concept of examining immersed features using electromagnetic waves is relatively new to space research, however, this is not the case as the final Apollo mission in 1972 made use of radar with a three-wavelength synthetic aperture of varying frequencies to examine the geological framework of the moon (Porcello et al. 1974; Sorsa 2021). Since then, there have either been proposed or completed missions in various years that have explored the use of radars in the exploration of space to examine immersed features of space objects (Asphaug et al. 2001; Haruyama et al. 2017; Kofman et al. 2007).

The first attempt to measure the internal frame of a Small Solar System Body was the COmet

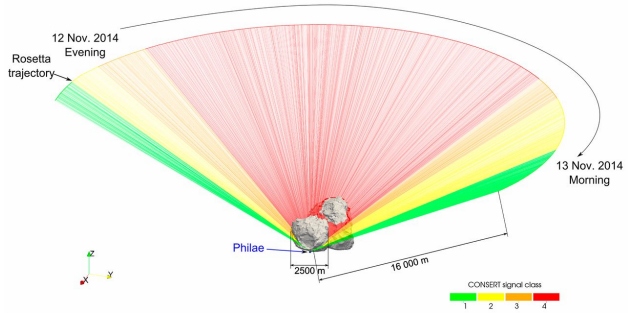

Figure 2.3 *Transmission of signal waves from Philae to Rosetta. colour code (1) strong SNR and good synchronization represented by the green colour, (2) acceptable SNR without synchronization represented by the yellow colour, (3) low SNR represented by orange colour, and (4) absence of signal represented by the red colour (Kofman et al. 2015)*

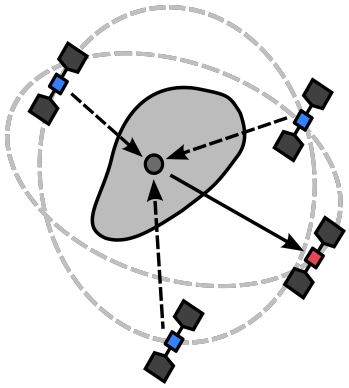

Figure 2.4 *A single receiver depicted by the red colour, records the transmitted signals separately by one or more than one orbiters depicted in blue (Pursiainen and Kaasalainen 2016).*

Nucleus Sounding Experiment (CONSERT) using Radio-wave Transmission, which was part of the European Space Agency's Rosetta mission to comet 67P/Churyumov-Gerasimenko (ESA). This mission made use of a bistatic radar instrument that propagated a signal which was transmitted across the lander Philae and an orbiter Rosetta (Kofman et al. 2015; Yusuf et al. 2021) and formed the basis for CTR in space research as we know it today. Figure 2.3 shows a transmission signal between the Philae and Rosetta as it navigates. In the research carried out by Pursiainen and Kaasalainen 2016, an advanced method for waveform tomography was proposed, it was suggested to produce an stimate for permittivity distributions while maintaining a fast computing time for 3D imaging. However, it left room for improving the robustness of the inversion method as well as a realistic implementation of the method proposed. In the research carried out by Sorsa et al. 2019 the methods proposed by Pursiainen and Kaasalainen 2016 were advanced and realistically showed that bistatic CRT can find cracks, deep interior voids and high permittivity boulders in an SSSB. Obviously, there is some room for further improvement as well, as several important ways to enchance the robustness of CRT were omitted this proof of concept study, e.g., the use of multiple radar frequencies.

2.5 Data Analysis and Modelling

The mining of valuable resources such as iron and gold dominated the 1800s. Oil drilling, natural gas, and shale oil extraction dominated the twentieth century. The twenty-first century has again seen the return of mining. However, this is a different kind of mining – the mining of data and today, data is unarguably the world's most significant intangible asset (Rossi 2015). The importance of data analysis in every industry cannot be overstated. Large data sets can be manipulated to assist any organization in identifying patterns and key insights that will lead to data-driven decision-making and improved business performance. This is also true in space research, where data analysis helps to identify patterns that lead to game-changing discoveries. A good example is the Galaxy Zoo project, which began in 2007 and aimed to classify approximately one million images gathered from the Sloan Digital Sky Survey for nearly a decade (Lintott et al. 2011). Its goal was to determine whether galaxies spin and what their shape and form are. It is common knowledge that the paucity of data and lack of computational power hindered the development of ground-breaking space technology. This narrative is rapidly changing, thanks to modern technologies like artificial intelligence, robotics and data science; an interdisciplinary field that combines numerical/statistical techniques with computational methods. Such technology has made it possible for spacecraft to manoeuvre autonomously, for scientists to identify the size of asteroids as they approach the planet, and to model space objects for various simulations and analyses.

3 Methodology

3.1 Overview

This chapter gives the details of the planning, the design and the methods used in implementing the printing of the 3D model of the asteroid Itokawa. It also describes the numerical models implemented to arrive at the ideal permittivity ratios and edge thresholds that were used in the model. The proposed model will enable scientists to have a better understanding of the interior properties of small solar system bodies, beginning with the asteroid Itokawa and thus help in simulating and planning future space missions, aid in planetary defence and provide a novel approach for future space mining.

3.2 Itokawa

The asteroid Itokawa is a small near-earth asteroid belonging to the S-type asteroid group. Hence, it has a stony composition and is said to be a rubble pile asteroid rich in magnesium and iron (Fujiwara et al. 2006). The exact shape of this asteroid was retrieved after a successful Hayabusa mission by JAXA in 2005 (Eyraud et al. 2020). Figure 3.1 is an image of the asteroid Itokawa which shows clearly that the asteroid has some rough surfaces as well as some smooth surfaces as well.

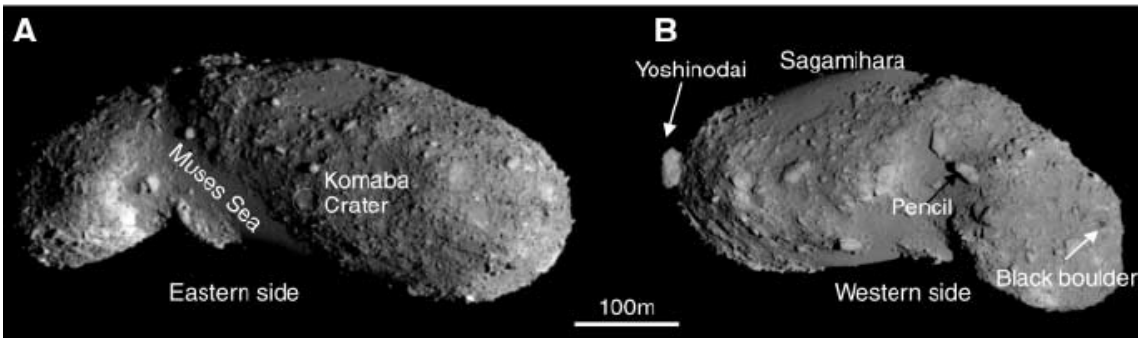

Figure 3.1 *Images of the asteroid Itokawa taken by JAXA's Hayabusa. It has a rough surface and inconsistent edges. (Saito et al. 2006)*

Itokawa appears to be composed of 100-200 m blocks and a thin regolith layer composed mainly of loosely aggregated stones and small round stones based on surface images provided by Hayabusa (Barnouin-Jha et al. 2008)

In this work, the intended analogue model will look like the Figure 3.1 and more importantly have ideal internal properties. Printing a 3D model of the asteroid Itokawa is a rather complex

task as the asteroid has an irregular surface.

3.3 Architecture

This section gives an overview of the process of the methodology. Figure 3.2 shows a flow chart of the whole process.

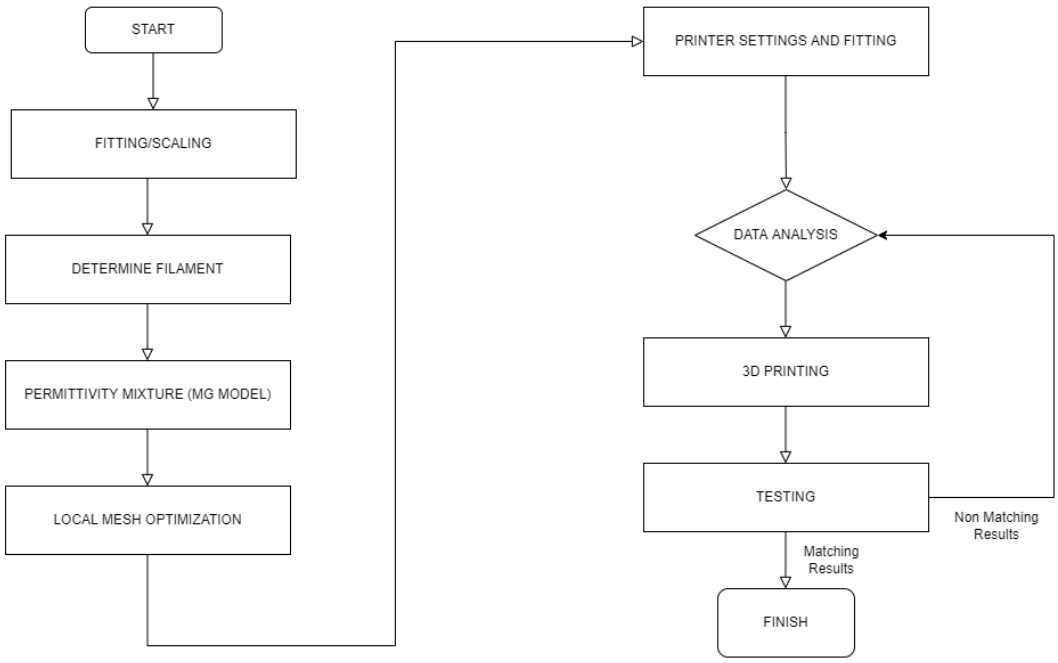

***Figure** 3.2 This figure shows the process of the main steps from start to finish of the final printed asteroid models.*

3.4 Methods

3.4.1 Fitting and scaling

This study uses the analogue scaling of (Sorsa et al. 2021b), where the 3D model was scaled from real size to laboratory size by choosing the peak size and weight of a model that can be fabricated seamlessly using a traditional 3D printer. This fitting process was also took into account that the target 3D model could be measured accurately in the anechoic chamber of CCRM (Common Microwave Resources Center), Fresnel Institute, Aix-Marseille University, CNRS, Marseille, France. In this chamber, the final measurements for the CRT will be carried out by placing the 3D model carefully on a polystyrene mast that is elevated and has the capacity to hold objects weighing a

few kilograms in size.

3.4.2 Material

3D-printable filaments Preperm ABS650 and ABS450, were used for this thesis work. These materials are commercially available proprietary Premix ABS technology-based special compounds which have been designed for extrusion but also have the capacity to accommodate injection moulding. They provide a stable dielectric constant with low losses over a broad frequency and temperature range (PREMIX 2019). As given by the manufacturer, these filaments have a diameter of about 1.75mm and a density of about 1.5g/cm^3.

With the permission of Vincent Laur, we estimate the permittivities of ABS650 and ABS450 based on the findings of Lab-STICC (Laboratoire des Sciences et Techniques de l'information, de la Communication et des Connaissances), CNRS, Brest, France, where permittivity measurements using 3D-printed control samples (flat rectangles with dimensions approximately 5-by-5-by-1 mm) were carried out. The results of these measurements are shown in 3.3.

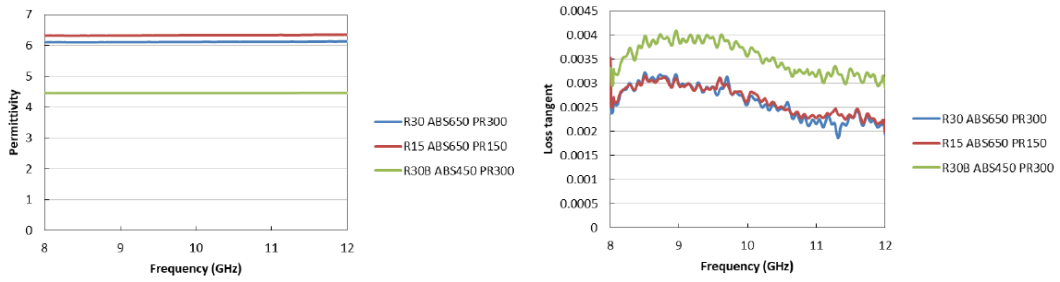

Figure 3.3 *In the results obtained with rectangular control samples (Lab-STICC), the measured permittivity is marginally lower than the permittivity values shown. This is due to the air present in the model. There is also a slight decline in density for the 0.30 mm 3D-printing resolution in comparison to the 0.15 mm.*

Permittivity Measurements				
Test Case	Filament/Resolution	Relative Permittivity		Density (g.cm$^-$3)
		Measured	Datasheet	
R30	ABS650/0.30	6.11	6.5	1.744
R15	ABS650/0.15	6.33	6.5	1.789
R30b	ABS450/0.30	4.45	4.5	1.484

Table 3.1 *Permittivity Dielectric characterization showing obtained measurements and data sheet reference.*

In the initial phases of this thesis, we have prepared numerical test objects such as a 3D-printed Stanford bunny and a 3D-printed Itokawa asteroid. The goal of the control sample measurement was to provide an initial or base value for permittivity calculations for varying filaments, and thus determine which filament provided the most effective results. Table 3.1 shows the results obtained from the lab in comparison to the results on the datasheet. We can observe that the measured

permittivity is marginally lower than the permittivity on the datasheet. We can also observe that there is a decline of about 3.5% in density for the R30 when comparing it to the R15.

Loss Tangent Measurements		
Test Case	Relative Permittivity	
	Measured	Datasheet
R30	0.0026	0.004
R15	0.0026	0.004
R30B	0.0035	0.004

***Table** 3.2 Loss Tangent Dielectric Characterization showing obtained measurements and data sheet reference.*

3.4.3 Mathematica model

In this work, we developed a mathematical model for steering the volumetric filling level of a 3D-printable tetrahedral wireframe, in which overlapping regular prisms $\{P_j\}_{j=1}^{m}$ substitute the edges of a tetrahedral mesh $\mathcal{T}$ of tetrahedra $\{T_j\}_{i=1}^{n}$, edges $\{E_j\}_{j=1}^{m}$ and nodes $\{N_\ell\}_{\ell=1}^{p}$. The cross-section of each prism is assumed to be a regular triangle with a side length w, i.e., the width of the prism, and surface area $\sqrt{3}/4w^2$. The overlap takes place in the nodes of the mesh, ensuring that the edges are joined in the 3D printing process. To obtain a suitable amount of overlap, the total length of prism P is set to be $|P| = |E| + sw$, i.e., the length $|E|$ of the original edge E corresponding to the prism is extended by sw with s denoting an overlap parameter (Figure 3.4). To determine a suitable value for s, we assume that in each node of the tetrahedral mesh the overlap is concentrated into a co-centric sphere with a diameter coinciding with the edge width w. The edge is assumed to penetrate that region by the effective length sw coinciding with the side length of a cube with a volume equal to that of the sphere, i.e.,

$$(sw)^3 = \frac{4}{3}\pi\left(\frac{w}{2}\right)^3 \quad \text{or} \quad s = \frac{1}{2}\left(\frac{4}{3}\pi\right)^{1/3}. \tag{3.1}$$

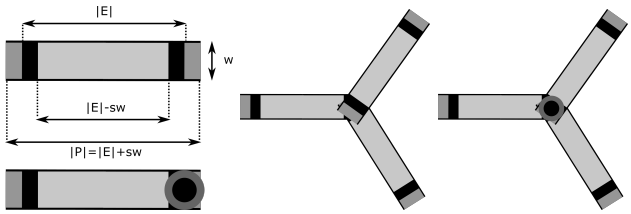

***Figure** 3.4 Overlapping prisms of the tetrahedral.*

3.5 Local mesh optimization

In order to allow tuning the local volumetric filling level of the wireframe according to a given distribution, we first define a binary-valued indicator function g which, given the sets A and B,

obtains the value one if A and B have one or more common points in common and is zero otherwise, i.e.,

$$g(A,B) = \begin{cases} 1, & \text{if} \quad A \cap B \neq \emptyset \\ 0, & \text{otherwise} \end{cases}, \tag{3.2}$$

and based on that, a tetrahedron- and node-wise weighting matrix $\mathbf{W^{(T)}}$ and $\mathbf{W^{(N)}}$ as follows:

$$\begin{aligned} W^{(T)}_{j,i} &= \sum_{k=1}^{n} d\frac{v_k}{v_i} g(T_k, E_j)\, g(T_i, E_j), \\ W^{(N)}_{j,\ell} &= \sum_{k=1}^{m} g(N_\ell, E_k)\, g(N_\ell, E_j). \end{aligned} \tag{3.3}$$

The first one of these is obtained by dividing the total volume of all the tetrahedra sharing the edge E_j by that of T_i. The second one equals the number of edges sharing E_j and the node N_ℓ.

We denote by v_i the volume of the i-th tetrahedron T_i, by f_i its volumetric filling, and by w_i the width of the j-th prism P_j. The total volume of the inflated edges in the mesh, not accounting for their potential overlap, matches that of the tetrahedra, that is

$$\mathbf{f} = \mathbf{V}^{-1}\mathbf{M}\mathbf{w}^2 \tag{3.4}$$

with $\mathbf{f} = (f_1, f_2, \ldots, f_n)$, $\mathbf{w} = (w_1, w_2, \ldots, w_m)$, $\mathbf{V} = \mathrm{diag}(v_1, v_2, \ldots, v_n)$, and

$$M_{i,j} = \frac{\sqrt{3}}{4|E_j| W^{(T)}_{j,i}}. \tag{3.5}$$

Because $\mathbf{M}$ is not a square matrix, the system cannot be directly inverted. However, the solution can be obtained approximatively via iterative relaxation, in this case, so-called Landweber iteration which takes small steps towards the residual as follows:

$$\mathbf{w}^2_\ell = \mathbf{w}^2_{\ell-1} + \delta \mathbf{M}^T(\mathbf{f} - \mathbf{V}^{-1}\mathbf{M}\mathbf{w}^2_{\ell-1}). \tag{3.6}$$

Here the user-defined relaxation parameter δ is chosen to be one ($\delta = 1$). After obtaining the solution of this system down to the relative tolerance of $1E-08$, the overlapping parts are taken into account via the following a fixed point iteration:

$$\mathbf{w}^2_\ell = \left(\sum_i \frac{(\mathbf{V})_{i,i}}{(\mathbf{S}\mathbf{w}^2_{\ell-1} - s\,\mathbf{T}\mathbf{w}^3_{\ell-1} + s\,\mathbf{J}\mathbf{w}^3_{\ell-1})_{i,i}} \right) \left(\sum_i (\mathbf{f})_i \right) \mathbf{w}^2_{\ell-1}, \tag{3.7}$$

for $\ell = 1, 2, \ldots$, a balance-condition for the total amount of material, that is iterated until the

relative tolerance of 1E-02 is reached. Here the matrices are given by

$$\begin{aligned} S_{i,j} &= \frac{\sqrt{3}|E_j|}{4W_{j,i}^{(T)}} \\ T_{i,j} &= \frac{\sqrt{3}}{4W_{j,i}^{(T)}} \\ J_{i,j} &= \frac{\sqrt{3}}{4W_{j,i}^{(T)}} \sum_{\ell=1}^{p} \frac{1}{W_{j,\ell}^{(N)}} \end{aligned} \tag{3.8}$$

and correspond, respectively, to the estimates of (1) total amount of material in the edges, (2) the overlapping parts of the edges, which are subtracted from the total amount, and (3) the total material in the edge junctions, which is based on the model of co-centric spheres and added to the difference of the first two material amounts.

Hence, the edge widths for a given tetrahedral mesh and volume fraction distribution is obtained in two stages (i) iterative relaxation which is followed by (ii) a fixed point iteration. This two-stage formulation was adopted, since a single-stage process turned out to be difficult to be stabilized numerically. The following sections analyze the errors related to this process.

3.5.1 Maxwell Garnett

Using the Maxwell Garnett (MG) model to determine the effective permittivity of a material mixture is not a new phenomenon as shown in the research efforts, e.g., in (Sihvola et al. 1985), where the Maxwell Garnett model was used successfully to determine the dielectric constant as well as the mixing formulae of snow. In this work, the Maxwell Garnett (MG) model is applied to determine the dielectric constant and mixing measures of the target asteroid model. The formula for the Maxwell Garnett (MG) model is given in equation 3.9 below where ε_{eff} is the medium's dielectric constant is ε_m, ε_i is that of inclusions (here the dielectric constant of the air $\varepsilon_i \approx 1$), and δ_i is the volume fraction of the inclusions.

$$\left(\frac{\varepsilon_{\text{eff}} - \varepsilon_m}{\varepsilon_{\text{eff}} + 2\varepsilon_m}\right) = \delta_i \left(\frac{\varepsilon_i - \varepsilon_m}{\varepsilon_i + 2\varepsilon_m}\right) \tag{3.9}$$

The dielectric constant is derived in the formula shown in equation 3.10.

$$\varepsilon_{\text{eff}} = \varepsilon_m \frac{2\delta_i\left(\varepsilon_i - \varepsilon_m\right) + \varepsilon_i + 2\varepsilon_m}{2\varepsilon_m + \varepsilon_i - \delta_i\left(\varepsilon_i - \varepsilon_m\right)} \tag{3.10}$$

3.6 Asteroid Wireframe Function

The complete working code for the Wireframe function(Pursiainen et al. 2020) was written in Matlab and is fully described in Appendix A. The function is designed to generate a prismatic surface mesh for 3D printing from a given volumetric tetrahedral mesh. The function is technically divided into several sections: initializing the parameters, mesh refinement, initialization for prism creation, matrix construction for finding the edge widths, finding the edge widths for a given filling ratio, and extending edges to set the overlap, and finally the refinement function.

3.6.1 Initializing the set parameters

In this code section, we begin by initializing the parameters by defining the argument. In the first function, the relative filling vector is generated. Furthermore, we loop through the length of the domain vector and we assign the filling vector auxiliary to the indices with those of the tetrahedra in the mesh.

3.6.2 Mesh Refinement

This is an optional code section and is only called upon request. If the number of mesh refinements is greater than zero then the mesh will be refined recursively number the given number of times. We loop through the length of the number of refinements and then assign previous nodes to the refined mesh nodes.

3.6.3 Prism Creation

In this section of the code, the main goal is to replace singular (linear) edge prisms constructed by triangular surface elements. The volume of each tetrahedron is first calculated by evaluating the determinant of each tetrahedron and then this information is then used to calculate the width that corresponds to the desired volumetric filling ratio. In the original tetrahedral mesh, each prism replaces one edge. Each one has a triangular cross-section and is made up of 8 different triangular faces: two triangular faces matching the edge and two triangles per rectangular edge connecting those two triangular faces. The Figure 3.5, shows a visual representation of this.

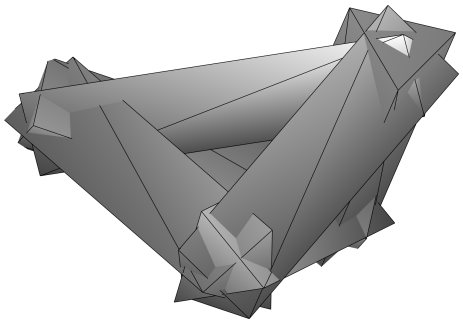

Figure 3.5 *An example of prism creation, showing how triangles are merged to form prisms and used as edges of a tetrahedron within the complex 2D model.*

3.6.4 Matrix Construction for Finding the Edge Widths

This code section is a part of the prism creation process, its purpose is to create the matrices needed in the iteration enabling a smooth running and calculation of the mathematical iteration described in Equation 3.8.

3.6.5 Extending Edges to Set the Overlap

This code section is also a part of the prism creation process and the final step. We have ensured that the edges have enough overlap to enable printing and avoid having voids or air gaps which can influence the permittivity ratio.

3.7 3D Printing

The process of turning a digital file into a three-dimensional object using a layer-upon-layer concept via a machine is known as 3D printing (Trust and Maloy 2017). The applications of 3D printing are numerous and it is commonly used to model the physical properties of various objects in areas such as medicine, retail and space exploration. In this work, we made use of this 3D printing technology to print the asteroid Itokawa model. The printing of these models was carried out in the FabLab at Tampere University Finland. In February 2022 the first models were printed and the second models were printed during the summer of 2022.

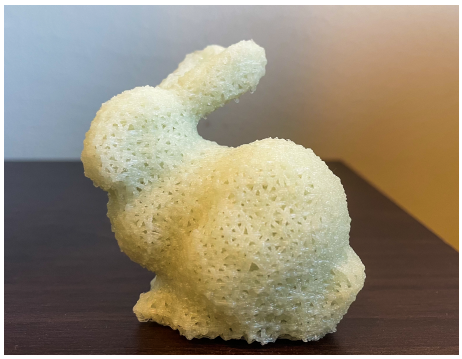

Figure 3.6 *Sample 3D model of the Stanford Bunny, printed at the initial stage to test the functionality of wireframe function at Fablab.*

3.7.1 Printer and Printer settings

In this work, the open-source PrusaSlicer software version 2.4.1 was used to fit the settings, slice the model and export files of the modelled asteroid to a gcode format that the Prusa 3D printer, Prusa i3 MK35+ recognizes for printing.

3.7.2 PrusaSlicer

The PrusaSclier is an open-source computer software that has so many rich features and is used to slice and export the ideal files for printing robust 3D objects. This software works seamlessly on the Mac, Windows and Linux operating systems (Prusa 2022). It also works seamlessly with the Prusa i3 MK 3 printer which is an improvement from previous printer models, hence the reason it was chosen for this thesis. The table 4.1 shows the Prusaslicer printer settings were used to obtain the target model of the asteroid Itokawa:

4 Validation of the Wireframe Function

To test the efficiency of the Wireframe Function, numerical validation is required. As a result, we considered the model's measured error, loss tangent, imaginary and real permittivities as well as the volumetric filling ratio, which is controlled by the edge width. The edge width and volumetric filling relationship enable the adjustment to the ideal permittivity of the model and therefore gives control of permittivity in complex structures. Furthermore, we obtained varying numerical results for three different sample sets; the first being without edge correction, the second with edge correction only, and the third with both edge correction and threshold. These results were obtained by slicing the models using the 3D printing software PrusaSlicer and its appropriate printer settings. The settings used for the printer are displayed in more detail in table 4.1.

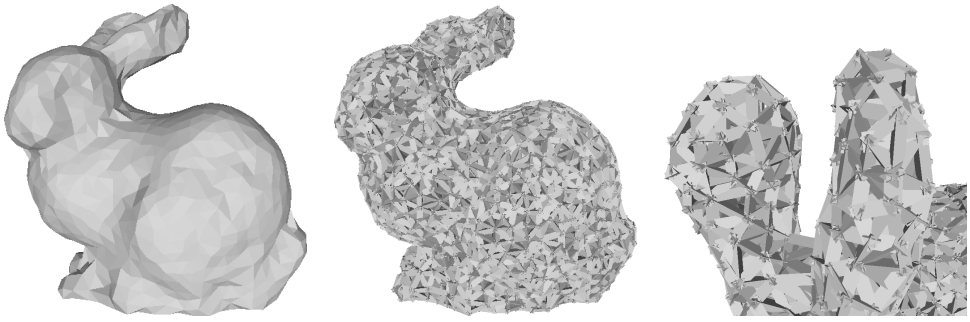

Figure 4.1 *3D Stanford Bunny stereolithography (STL) with varying model properties such as edge threshold, filing levels, and printer properties.*

PRINTER PARAMETERS	SETTINGS
Nozzle	Single
Nozzle Diameter	0.4mm
Raft Layers	2
Layer Height	0.3mm
Nozzle Temperature	245-250 °C
Plate Temperature	100-110 °C
Fill Density	15%
Fill Pattern	Gyroid
Filament	ABS450
Skirt Height	3 Layers
Brim type	Outer Brim
Perimeter Extruder	1
Infill Extruder	1
Initial Print Speed	70%
Draft Shield	Enabled

Table 4.1 *Settings used on the Pruserslicer software ranging from temperature parameters to the nozzle sizes as well as the density for printing the asteroid models.*

4.0.1 Printed Objects

In this thesis, we printed the Itokawa model, the KY model, Stanford bunny and the spheres using different filling levels and printer settings in order to arrive at the optimal final print. Figure 3.6, Figure 5.6 and Figure 6.3 show visual representations of these models

4.1 Computational Methods

The following computational methods have been implemented in this work. The simulation was run using the programming language Matlab on a Dell computer which consists of hardware with 16-core processors and 256 GB RAM worth of memory. Data analysis and data visualizations were carried out using Matlab. Some figures were also designed using the free software GNU Image Manipulation Program (GIMP) version 2.10.30.

4.2 Numerical Validation

In Figure 4.1, To test the functionality of the wireframe function, we printed several samples of the Stanford bunny. We chose the Stanford bunny because it is a complex shape with varying surfaces, and its STL is high resolution and freely available online. We obtained the STL file from the Stanford University Computer Graphics Laboratory's repository.

Case descriptions			
Properties	CASE I	CASE II	CASE III
Filling level	0.95	0.95	0.95
Printer resolution	0.15 mm & 0.30 mm	0.15 mm & 0.30 mm	0.15 mm & 0.30
Edge resolution	0	0	1.2
Volume	66292	66292	66292

Table 4.2 *Model properties by different case descriptions, showing different tests for the effects of correction and thresholding. Applying either correction or thresholding, both scenarios or none of those.*

4.3 Results

This section focuses on asteroid simulation and parameter estimation for realised permittivity ratios using the Maxwell Garnett method, the PrusaSlicer, and a wireframe-creating Matlab code (Appendix). The estimation method was also extended to asteroid data obtained from two different labs. Jean-Michel Geffrin's results from CCRM, Marseille and our numerical findings at Tampere University will be used for this analysis, respectively. In this section, we will go over the procedures for simulating and estimating the parameter. The estimates' results and error margins in the estimated parameters will also be presented and discussed.

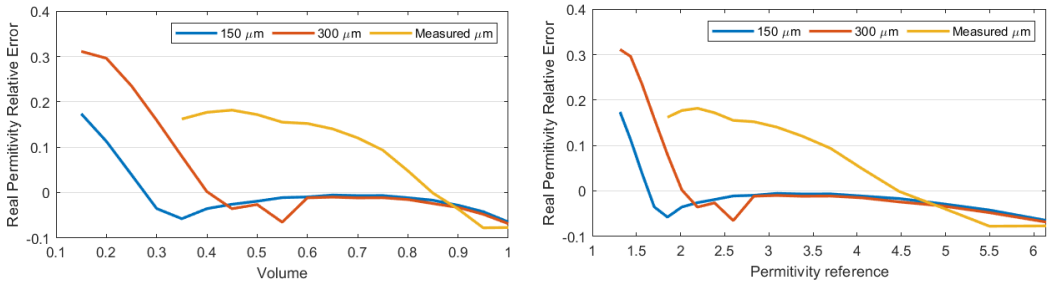

Case (I): When edge threshold but no correction has been applied.

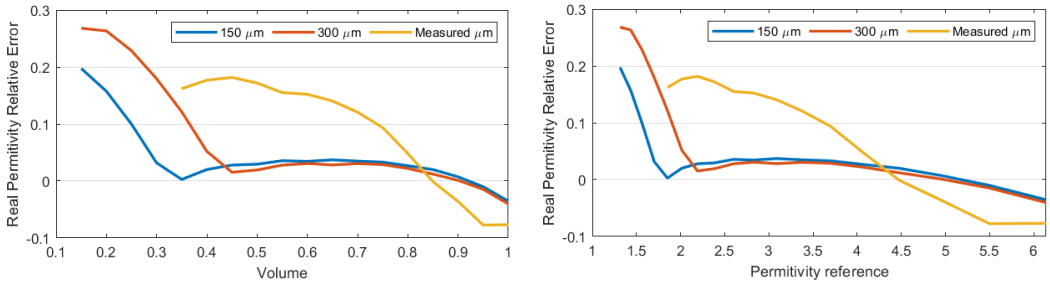

Case (II):When both correction and edge threshold have been applied.

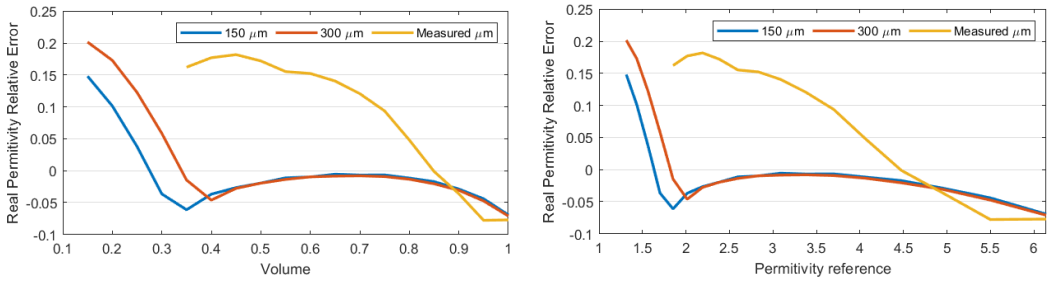

Case (III): When neither correction nor edge threshold has been applied.

***Figure** 4.2 This figure depicts the numerical results obtained for the cases I-III showing two different printing resolutions and a value measured by Jean-Michel Geffrin at CCRM for a 35 mm diameter sphere. The relative error estimates have been calculated using the Maxwell Garnett model as the reference. The filling levels of the numerically modelled objects have been estimated based on sliced data obtained with Prusa Slicer. The blue curve represents the resolution at 0.15 mm, the red curve represents the resolution at 0.30 mm and the yellow curve shows the measured results showing the variation in the real permittivity error in comparison to the volume and permittivity reference.*

4.3.1 Numerical Results

We divided the data into three cases in this section: case 1 when edge threshold but no correction was applied to the mesh, case 2 when both correction and edge threshold was applied to the mesh, and case 3 when neither correction nor edge threshold was applied to the mesh. By slicing the 3D model with the PrusaSlicer software, this segmentation was achieved. In general, for all curves, the thresholding effects primarily impacted the left side of the figures where the explosion occurs, while the correction effect primarily impacted the right side of the figures. To ensure that the

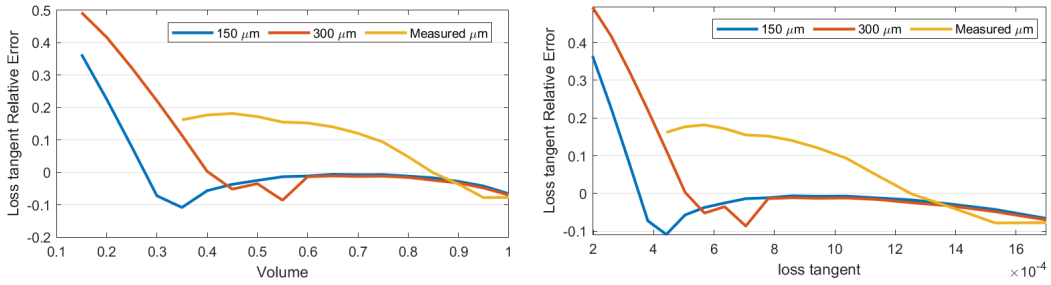

Case (I): When edge threshold is applied but no correction.

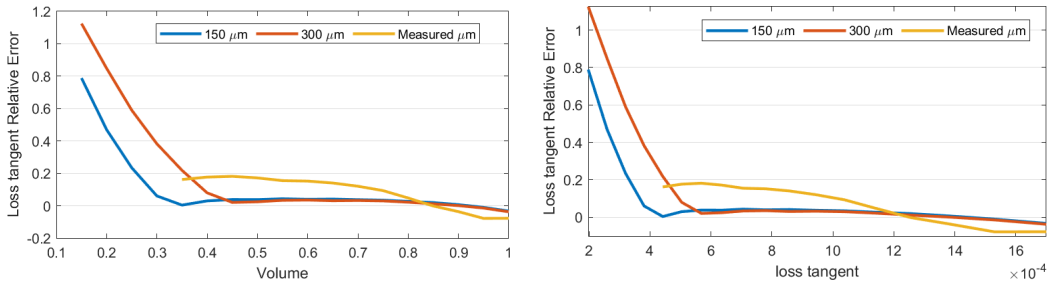

Case (II): When both correction and edge threshold have been applied.

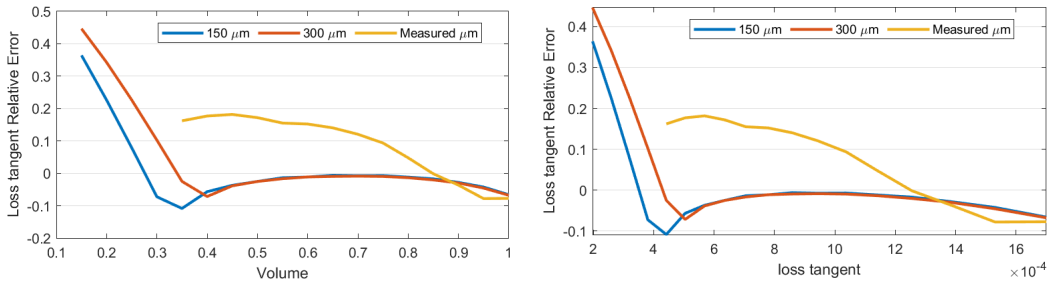

Case (III): When neither correction nor edge threshold has been applied.

Figure 4.3 *This figure depicts different case values (I-III) showing two different printing resolutions and an experimental value measured by Jean-Michel Geffrin at CCRM for a 35 mm diameter sphere. The relative error estimates have been calculated using the Maxwell Garnett model as the reference. The filling levels of the numerically modelled objects have been estimated based on sliced data obtained with Prusa Slicer. The blue curve represents the resolution at 0.15 mm, the red curve represents the resolution at 0.30 mm and the yellow curve shows the measured results showing the variation in the variation in Loss tangent relative error in comparison to the volume and loss tangent.*

printer does not misinterpret edge sizes, it was necessary to threshold out the edges that are too thin to be printed and add some width (correction) to the edge.

Real permittivity

In all cases, we compared the measured permittivity to the data visualized with the real permittivity error as the y-axis and the volume and permittivity reference as the x-axis for two different printer resolutions.

Case 1: Figure 4.2 shows that we cannot achieve low permittivities below 0.3; the relative

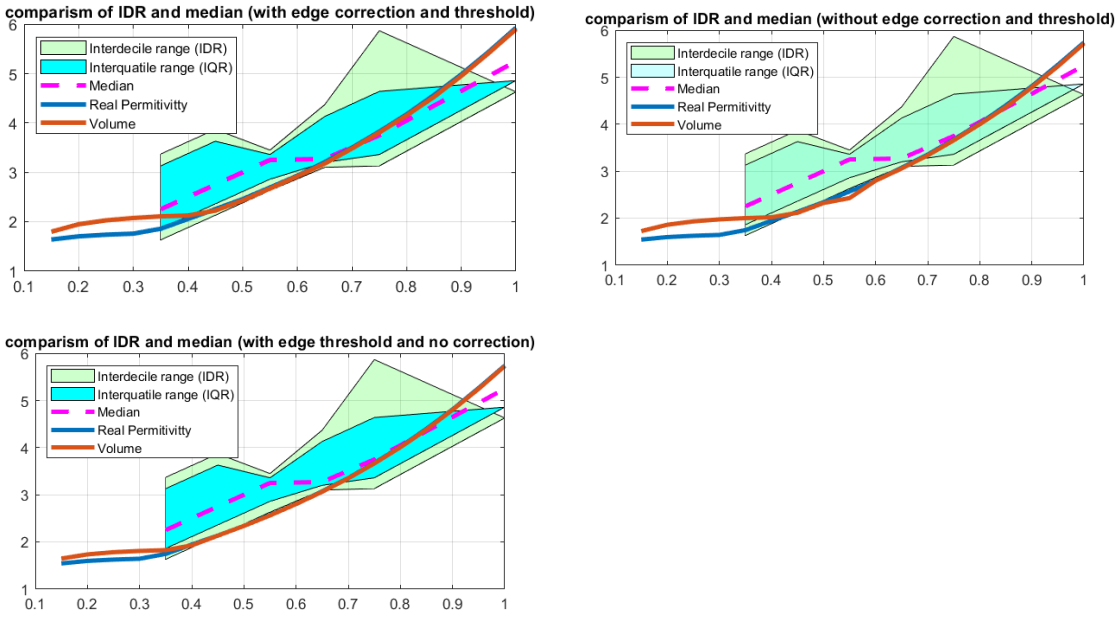

Figure 4.4 *This figure depicts the comparisons of the numerical results with the experimental data (2–18 GHz) measured by Jean-Michel Geffrin at CCRM for 35 mm diameter spherical test objects. The comparison is shown for the following three cases: with correction and threshold, without correction and threshold and with correction and threshold.*

error always increases when the volume fraction decreases below that point. We also notice a sudden increase in relative error, which is caused by the edges failing to print properly due to the threshold and limited printer resolution. The best fit with the measured data is suggested to be around 4.5. Given that the measured value depicted by the yellow curve includes not only the printing error but also the measurement error, it has more errors than the simple models depicted by the red and blue curves that were created numerically. When we compare the yellow curve to the other curves, we can see that the percentage margins for error are around 0.5.

Case 2: The volume case yields a similar result to the first case in that we also cannot achieve low permittivities below 0.3; the volume fraction decreases as the relative error increases. The best fit with the measured data is suggested to be around 4.5 as well. Again the depiction of the yellow curves which reflect the measured values includes both measurement and printing errors, hence it has more errors than the numerically generated simple modelled blue curves. This case is also present in Figure 4.2. The main difference between other cases is that each curve is slightly lifted and this leads to a correction for the high filling ratios.

Case 3: In this case neither the edge threshold nor the correction has been applied. The curves although similar to the others show the lowest curve values. We can see that we also cannot achieve low permittivities below 0.3; the volume fraction decreases as the relative error increases. The best fit with the measured data is suggested to be around 3.9. This case is also referenced in Figure 4.2.

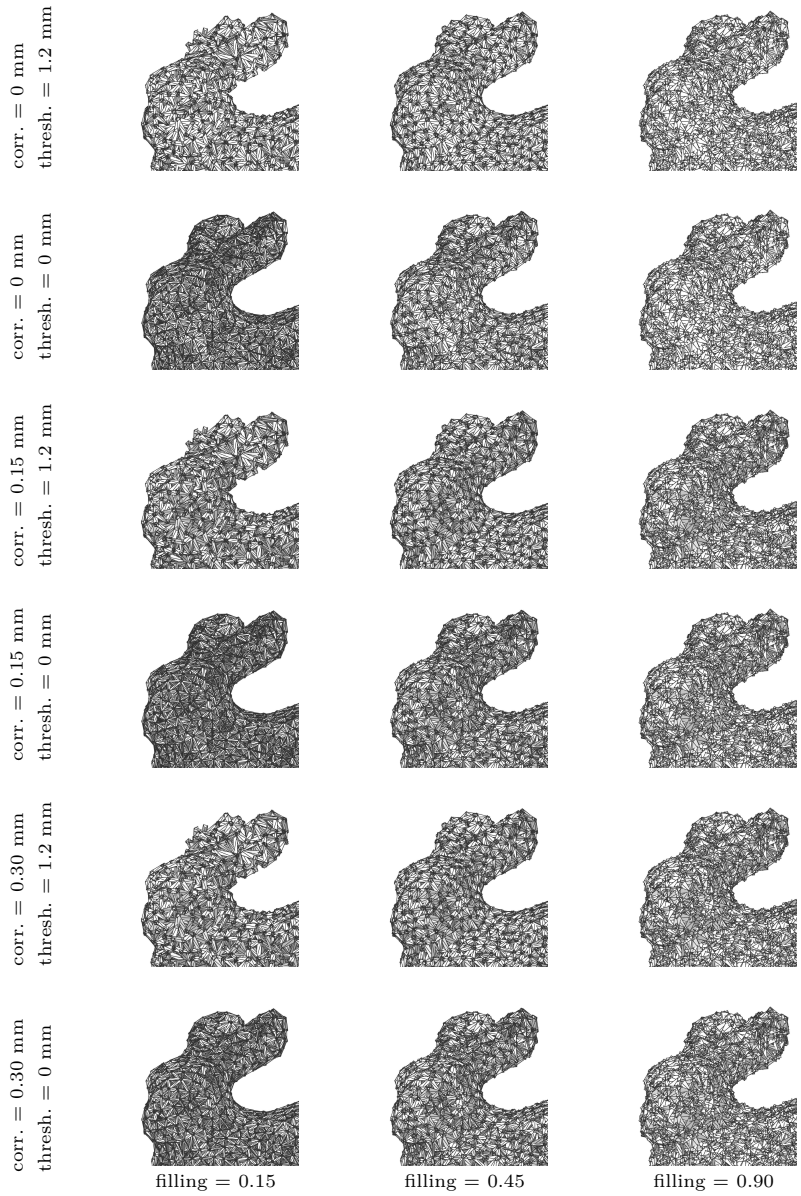

Figure 4.5 *This figure depicts a 3D Stanford bunny with varying filling levels showing mesh edges and surface smoothness.* ***Left:*** *Filling level 0.15.* ***Middle:*** *Filling level 0.45.* ***Right:*** *Filling level 0.90.*

LOSS TANGENT

In this section, we also compared the measured permittivity to data visualized with the loss tangent relative error as the y-axis and the volume and loss tangent as the x-axis for 2 distinct printer resolutions in all cases.

Case 1: Considering that the measured value illustrated by the yellow curve contains both printing and measurement errors, it contains more errors than the simple numerical models depicted by the red and blue curves. When we compare the yellow curve to the others, we see that the percentage margins of error are very close to point zero. Figure 4.3 shows that we cannot achieve

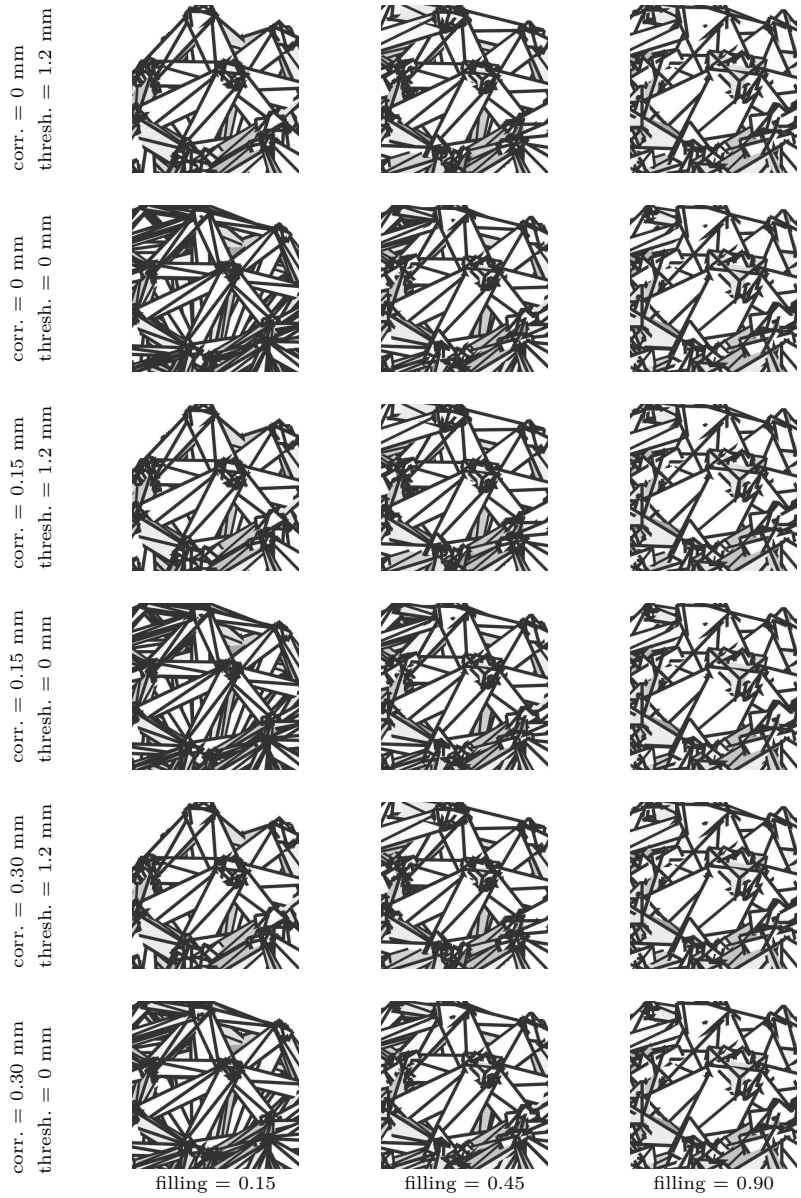

Figure 4.6 *Zoomed 3D Stanford Bunny at varying filling levels showing mesh edge, surface smoothness and overlap.* ***Left:*** *Filling level 0.15.* ***Middle:*** *Filling level 0.45.* ***Right:*** *Filling level 0.90.*

low permittivities below 0.4; the loss tangent error always increases when the volume fraction decreases below that point.

Case 2: Although the curves in this case presented in Figure 4.3 are similar to those in the other cases, the main difference between them is that each curve is slightly lifted, which results in a correction for the high filling ratios. In general, the overall level of the curve has a variable filling rate and can adapt in volume, with a near-zero error rate. It is suggested that the best fit with the measured data is around 4.5.

Case 3: This case is also referenced in Figure 4.3 shows that neither the edge threshold nor the correction has been applied. The curves although similar to the others show that the error

rate is very close to zero.

4.3.2 Numerical vs Experimental Results

We compared the interdicile and interquartile ranges, the median, real permittivity, and the volume for the three cases to show a comparison between the real and imaginary values of the model in figure 4.4. The purple dotted line represents the median values, the red line represents volume, the dark blue line represents real permittivity, and the blue and green areas represent interquartile and interdecile ranges, respectively. In general, we see a similar trend in all three cases, but after closer observation, we see that in the case in which both edge threshold and correction have been applied, the curves are lifted and closer to the median values than in the other cases, whereas in the case without edge threshold or correction, we see lower curves for real permittivity and volume, as well as a variation at 0.55. As a result, one can conclude that the corrected and edge-thresholded case fits the imaginary part far better than other cases.

Bunny Models

Figure 4.5 shows a selection of bunny images sliced with varying parameters in order to find the best match to print the 3D model. In general, the images show a Stanford bunny model sliced in three ways: first without edge threshold and correction, then with edge threshold and no correction, and finally with both correction and edge threshold applied. Overall, we see how correction and thresholding smooth out the images. We also notice that the first column, which contains images with a filling level of 15, generally has rougher surface edges.

Zoomed Bunny Models

Figure 4.6 depicts a variety of zoomed-in bunny images sliced with varying parameters. It depicts how the edge nodes of different cases overlap. The cases have been sliced in three ways, as shown in Figure 4.5: first without edge threshold and correction, then with edge threshold and no correction, and finally with both correction and edge threshold applied. Regardless of the correction or edge width applied, the filling level .90 shows a very disorganized layout of the edges, whereas .15 and .45 are more evenly spread. We also notice that the surfaces are larger when the 30 corrections is used instead of 15.

4.4 Mathematical Modelling and Data Analysis

To build an object for use in upcoming space missions and lab examinations, we used a mathematical modelling strategy. To create a numerical object, we initially merged a mathematical

model with a modelling study and then later realized this using 3D printing as a manufacturing technology to make the product.

5 Lab Validation

5.1 3D Model Generation

Figure 5.1 and Figure 5.2 show different cut angles of the Itokawa and Ky asteroid models respectively. These images show what is inside the asteroid; the voids and cracks as well as the various layers.

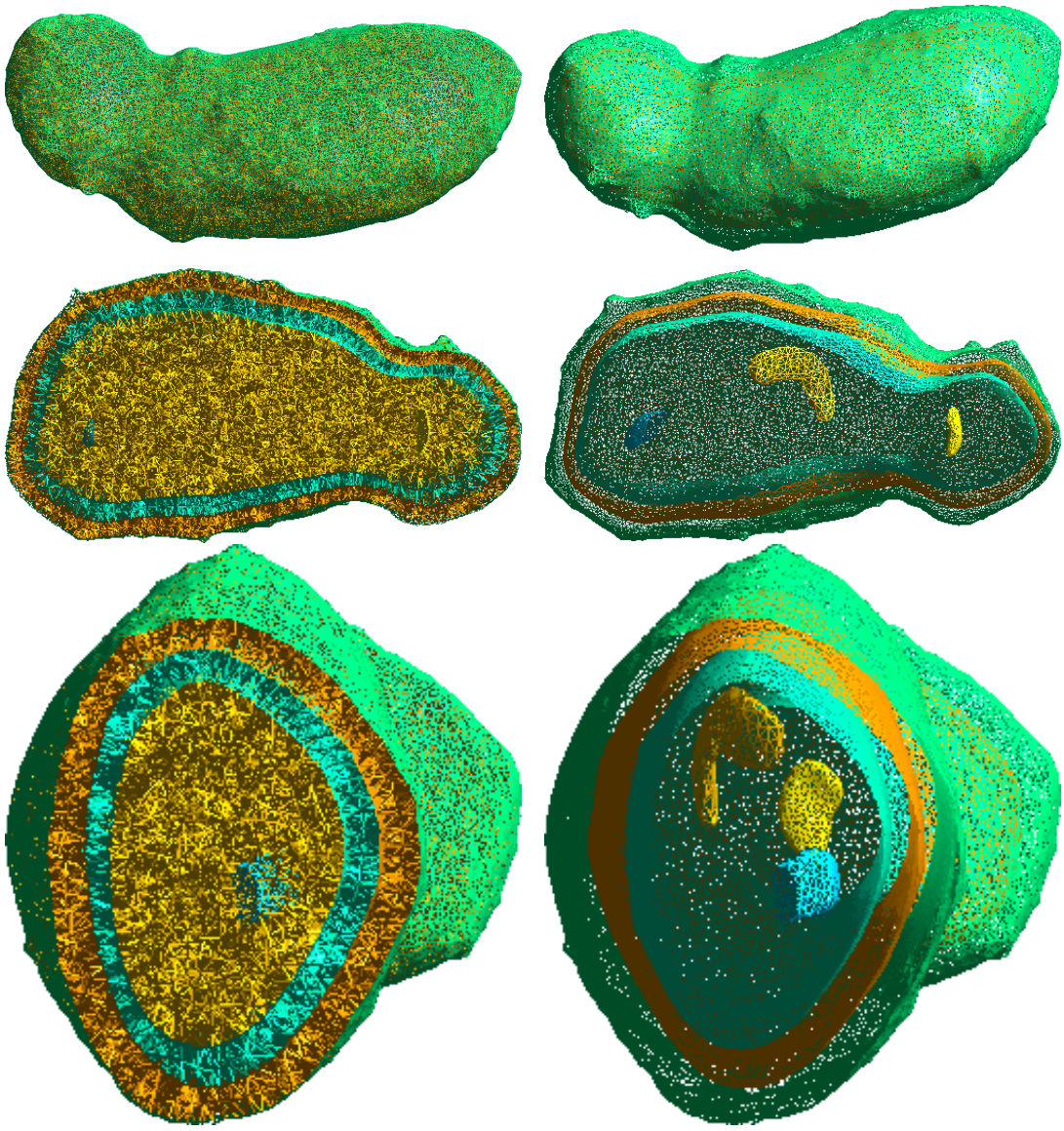

Figure 5.1 *This figure depicts three-dimensional and two-dimensional cuts of the model showing the voids and cracks embedded in the interior.*

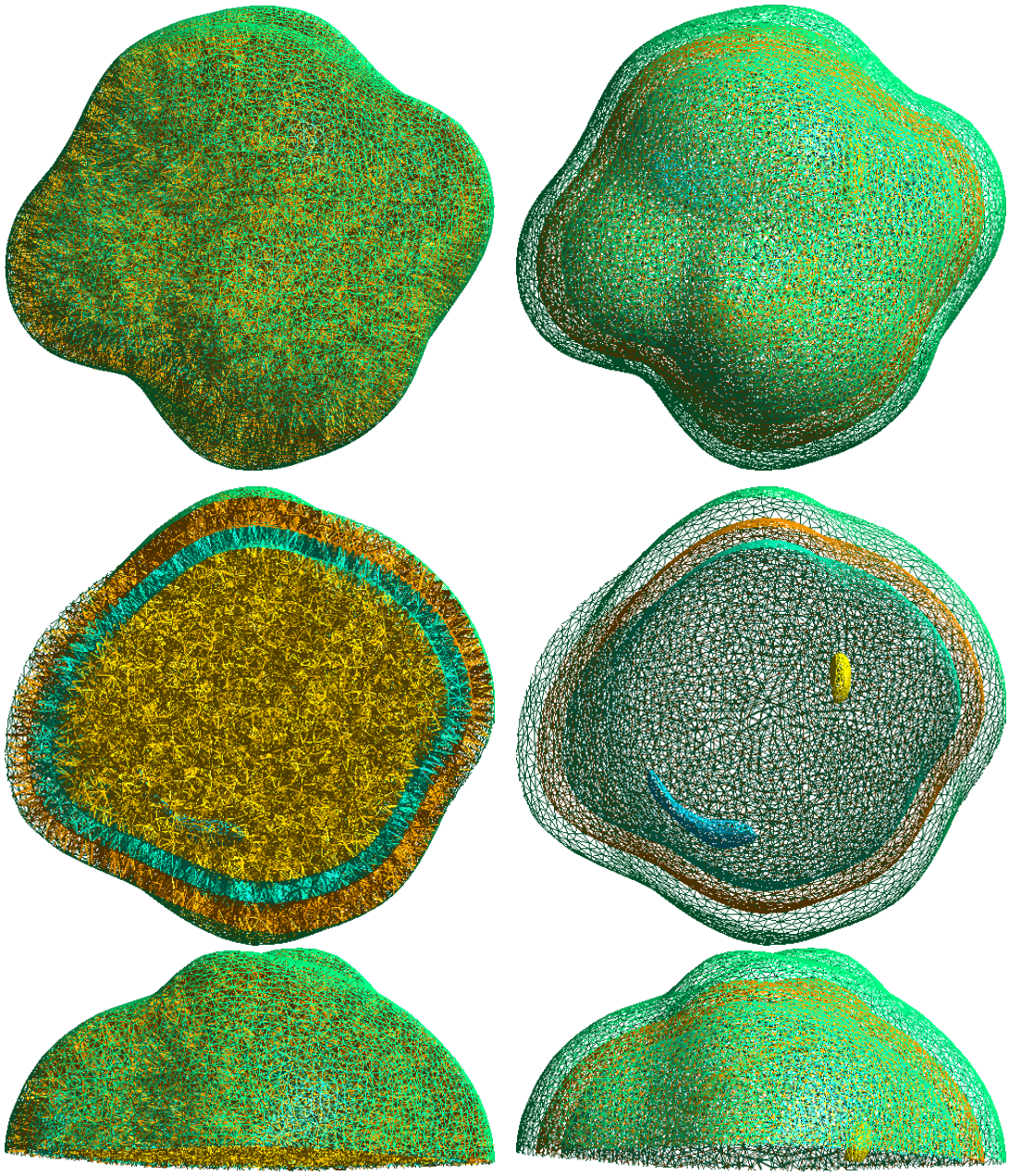

Figure 5.2 *This figure depicts* ***Left:*** *three-dimensional and* ***Right:*** *two-dimensional cuts of the KY model showing the voids and cracks embedded in the interior.*

5.2 Itokawa Shape Model

The Itokawa model was extensively examined in this thesis, showing different apertures, fractures and layers. This allowed for a more thorough compartmentalization of the models to match the specified permittivity ratios with filling ratios.

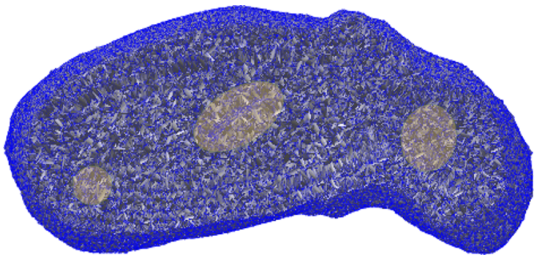

Figure 5.3 *This figure depicts three-dimensional cuts of the Itokawa model showing the voids and cracks embedded in the interior.*

5.3 KY Shape Model

Although the Itokawa model was the central focus of this research, we also examined the 1998 KY model. Similar to the Itokawa model, the models were created with a wireframe that was based on the tetrahedral mesh. This allowed for a more thorough compartmentalization of the models to match the specified permittivity ratios with filling ratios.

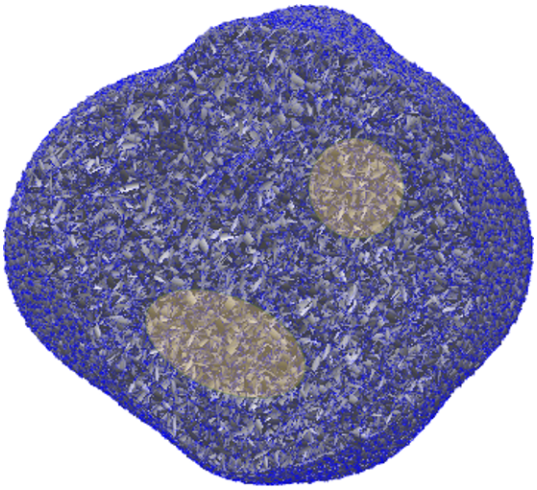

Figure 5.4 *This figure depicts three-dimensional cuts of the KY model showing the voids and cracks embedded in the interior.*

5.4 Interior Model

Based on the research carried out by Sorsa 2018, we see that an asteroid is likely to have a crack, boulder or single cavity and less likely to contain only a void, in this thesis we have further researched. Figure 5.1 shows various angles of the model

5.5 Layers and Cavities

In this thesis work, we depicted three distinct yet similar asteroid layers which contain different cavities and fractures. Figures 5.1 and 5.2 show a visual representation of this. We made fractures,

which are flat objects with a diameter in one direction less than $\lambda/2$ (wavelength divided by two), making them almost undetectable in a back projection or other linear radar reconstruction.

Equipment from the French laboratory CCRM, Marseille, were utilized to measure this. The measurement setting allowed a frequency range coverage of approximately 2 GHz to 18 GHz.

5.6 Tetrahedral Mesh Generation

The metamaterial selected to represent the makeup of asteroids and was used in creating the models is the tetrahedral wireframe which has a sophisticated structure. As shown in Figure 4.6 which was referenced earlier, the mesh was created using overlapping prisms and thus decreasing the error margins.

Filling Level	Reference	Derived
2.5	0.5314	0.5227
3.5	0.7246	0.7149
4.5	0.8583	0.8239

Table 5.1 *This table depicts the various filling levels used in printing the models, as well as their reference and obtained values.*

5.7 Wireframe Generation

In this thesis, the wireframe was created in a way that would produce the best print results for the model. The edge length, which varies somewhat within each wireframe, directly affects the sizes of the voids and edge widths. The filling ratios fr=0.45 and fr=0.90 were chosen with the following values, resulting in wireframe voids with a diameter of 1.4mm or less.

5.8 Experimental Objects

In this thesis, we present a model that outperforms the one previously employed to create the analogue by automating the process. The algorithm detects the filling levels automatically, and it enables manipulation of the printer resolution corrections and edge threshold, thus accounting for every little detail. In order to analyze the outcomes, actual data from a CCRM was also employed. Therefore, filling levels can be modified to the required specifications. The desired filling level and the actual filling level match, and the permittivity based on the radar test matches fairly well as well. To this effect, we have also calculated the degree of uncertainty. In order to check the various permittivity compartments, which have three different layers in the Itokawa model, we have created a dataset that can be used to build 3D printable analogues of them. Since the Itokawa model's individual layers were all printed as spheres, we have ensured that there is a way to roughly estimate the model's permittivity. As a result, we have a reference point for the potential structure and permittivity of the model, as well as data that makes measurement and comparison easier.

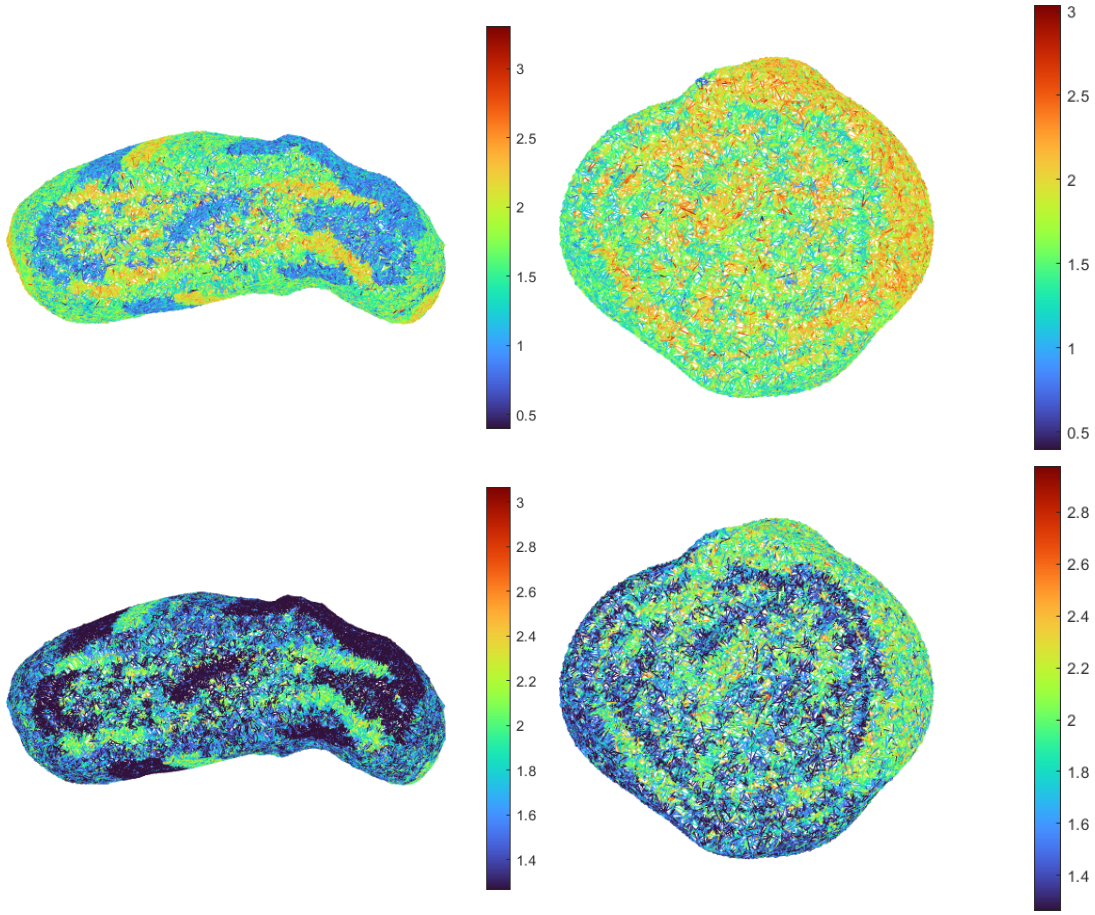

Figure 5.5 *This figure depicts the tetrahedron volume distribution in* mm^3 *for both the KY and Itokawa models.* ***Top:*** *Without threshold.* ***Bottom:*** *with the threshold.*

Figure 5.6 shows the filling level used to print each sphere using both the ABS 650 and the ABS 450 material.

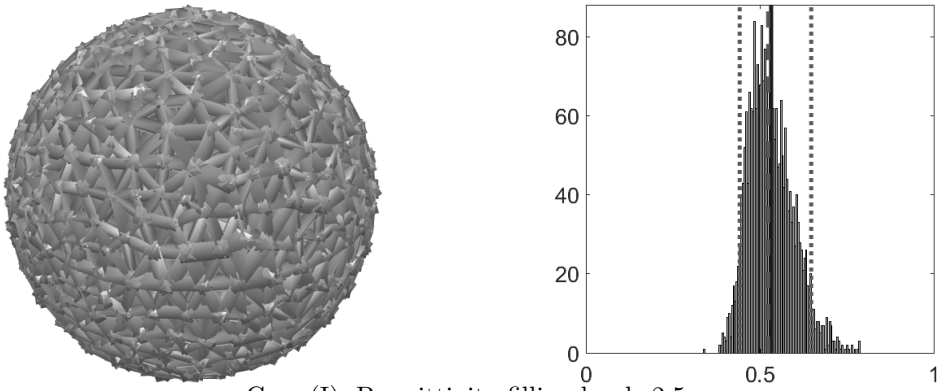

Case (I): Permittivity filling level: 2.5.

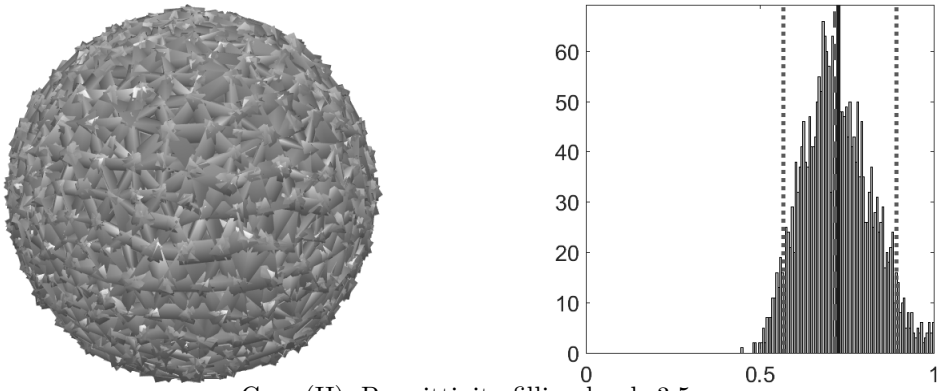

Case (II): Permittivity filling level: 3.5.

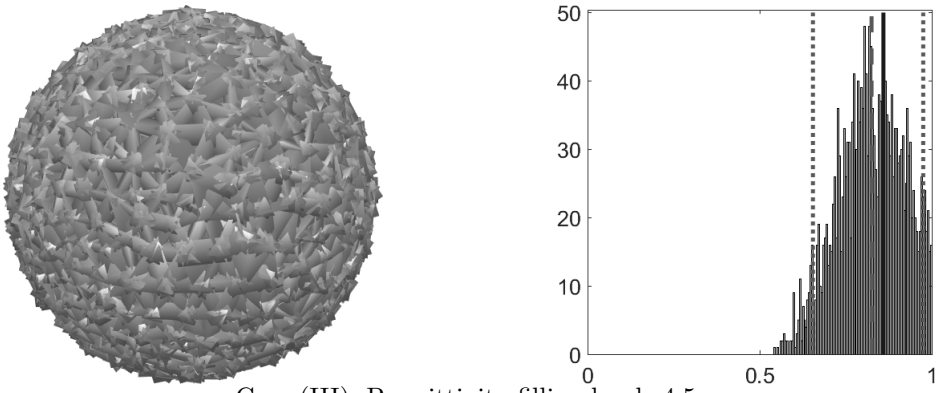

Case (III): Permittivity filling level: 4.5.

Figure 5.6 *This figure shows images of numerically simulated 35 mm diameter spheres with three different filling levels. Each histogram shows a comparison between numerically estimated element-wise filling levels and the targeted value. The vertical lines correspond to the end points of the 90 % credibility interval.*

6 Results of Lab Validation

6.1 Accuracy Analysis

Figure 6.1 and Figure 6.2 show graphs of the accuracy analysis of both the Itokawa model and the KY model respectively.

6.2 Tools and Resources

The following tools and resources were utilised during the process of this thesis work.

TOOLS & RESOURCES	TYPE/VERSION
Printer	Original Prusa i3 MK3+
GPU	Nvidia Quadro RTX 4000
CPU	Dell Precision Tower 5820
Software for Data Analysis	Matlab
Software for 3D Model Slicing	PrusaSlicer
Software for Image Editing	GIMP
Resource for Thesis Writing	Overleaf
Operating System	Windows 11
Print Location	FABLAB TUNI
Experimental Filament	PLA & ABS 650
Final Filament	ABS 450
Camera	iPhone 12 mobile camera
RAM Used	256 GB

Table 6.1 *The following tools and resources were utilised to complete this thesis, including software, computer models, and editing tools.*

6.3 Printing Process

This section gives details about the printing process. The Original Prusa i3 printers, which are the most popular Prusa printers, were utilized in Fablab at Tampere University. Additionally, we repeatedly utilized ABS 650 filament to print a few trial models that turned out to be challenging and unsuccesful before switching to ABS 450 filament to produce the final print, which was printed at a temperature of approximately 245 degrees Celsius. Each trial model took about six days to print and the final print took 7 days. We set up a system to support the filament continuously throughout the printing process and enabled the draft shield, which helped to retain some heat and prevent cracks, in order to prevent layer shifting, which occurred during the printing of the prior test models. Figure 6.3 shows images of the printers.

6.3.1 Experimental Printing Process

Since ABS filament is more expensive and takes longer to print the models we decided to utilize a less expensive printing filament called PLA that is simpler to print and more sturdy in order to test the functionality of the final model. In order to confirm that the procedure worked not only

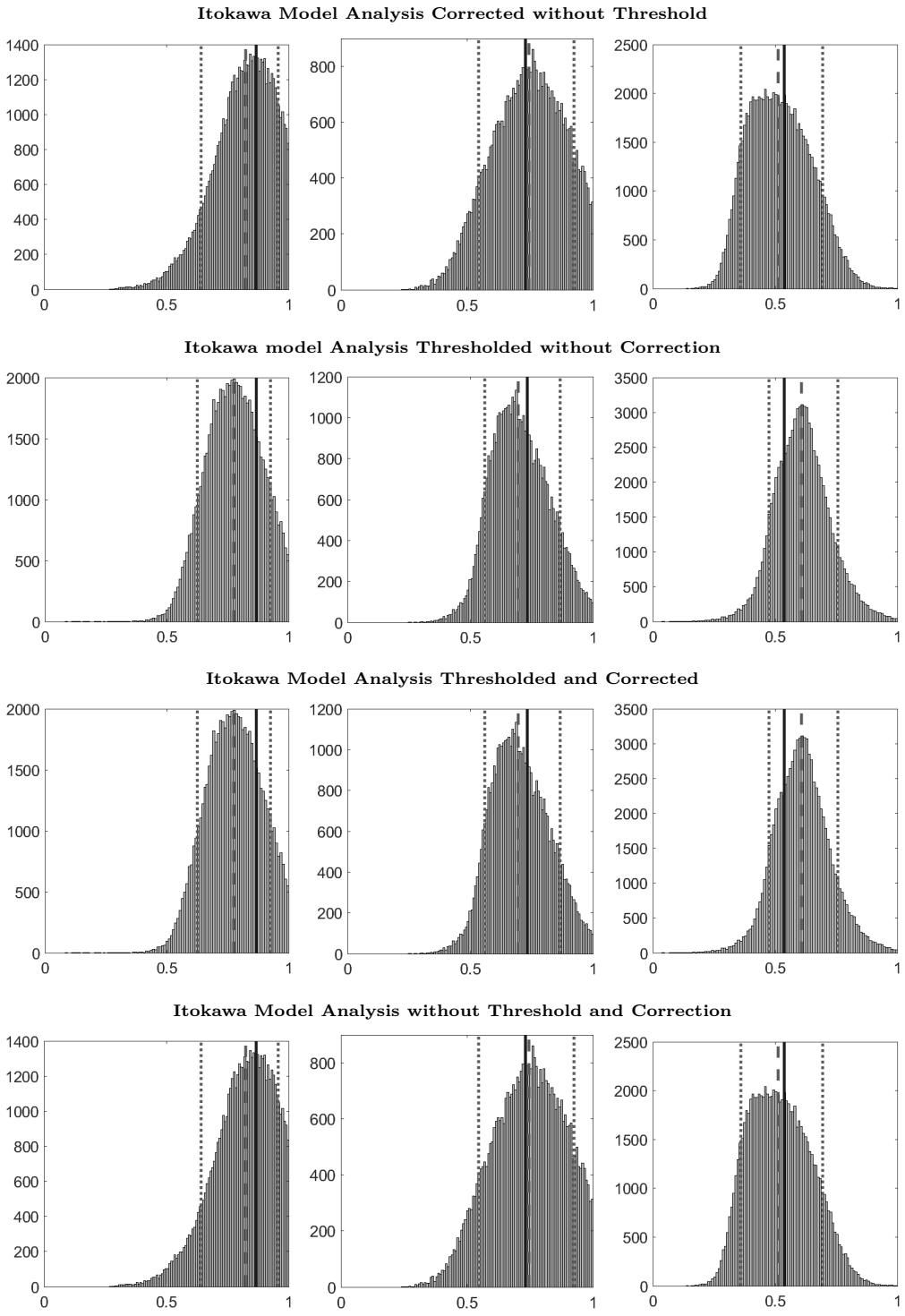

Figure 6.1 *Representations of the analyzed results for the Itokawa model. Each histogram shows a comparison between numerically estimated element-wise filling level and the targeted value. The vertical lines correspond to the end-points of the 90 % credibility interval.* ***Left:*** *Filling level 0.15.* ***Middle:*** *Filling level 0.45.* ***Right:*** *Filling level 0.90.*

for one asteroid model but also for others, we also made the decision to print both the KY and Itokawa asteroid models experimentally. During the experimental printing process, the layers and fractures that were built into the model were clearly visible in both the Itokawa and KY models.

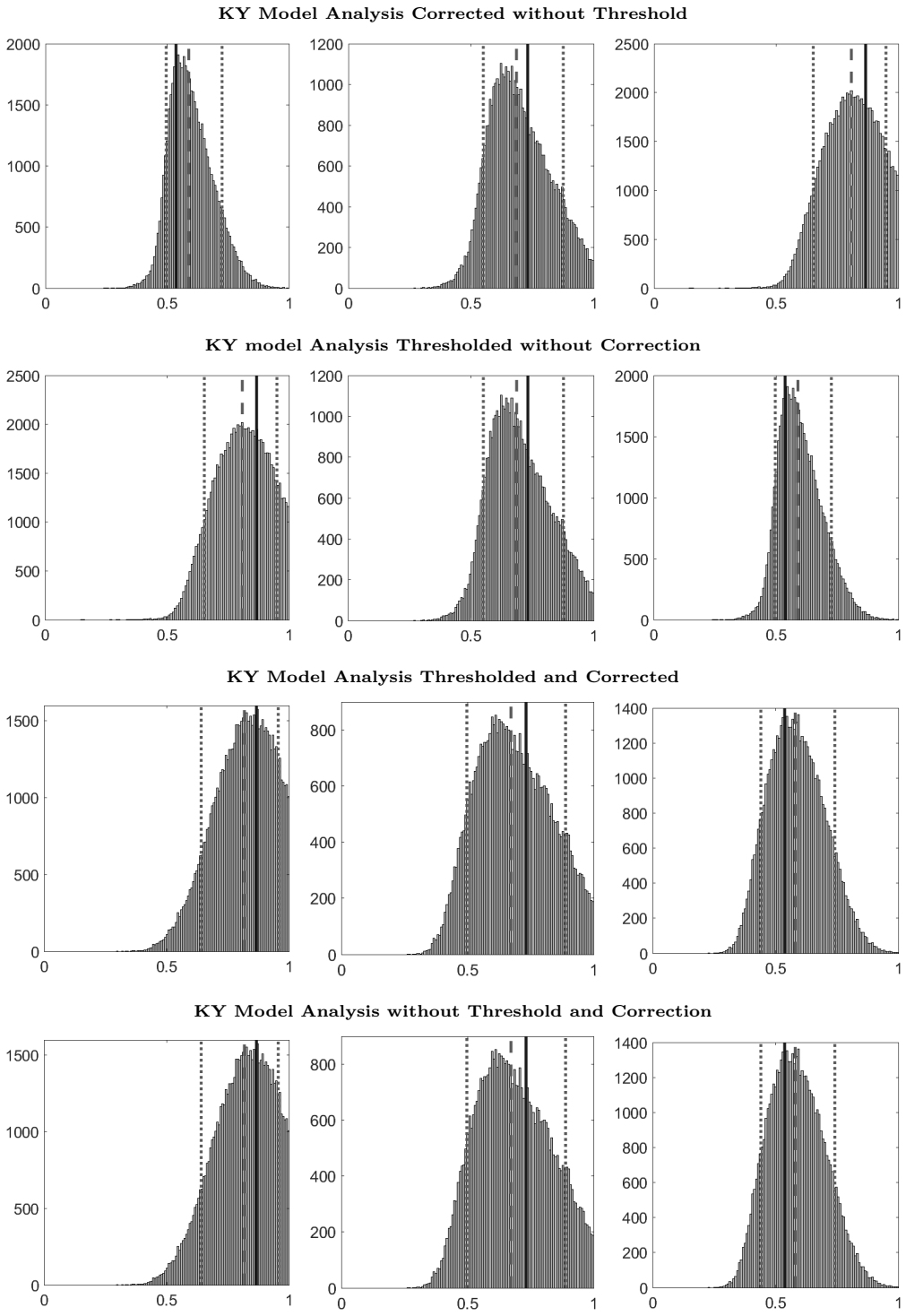

Figure 6.2 *Representations of the analyzed results for the KY model. Each histogram shows a comparison between numerically estimated element-wise filling level and the targeted value. The vertical lines correspond to the end-points of the 90 % credibility interval.* ***Left:*** *Filling level 0.15.* ***Middle:*** *Filling level 0.45.* ***Right:*** *Filling level 0.90.*

Images of the printing process are shown in Figures 6.4, 6.3 and 6.5.

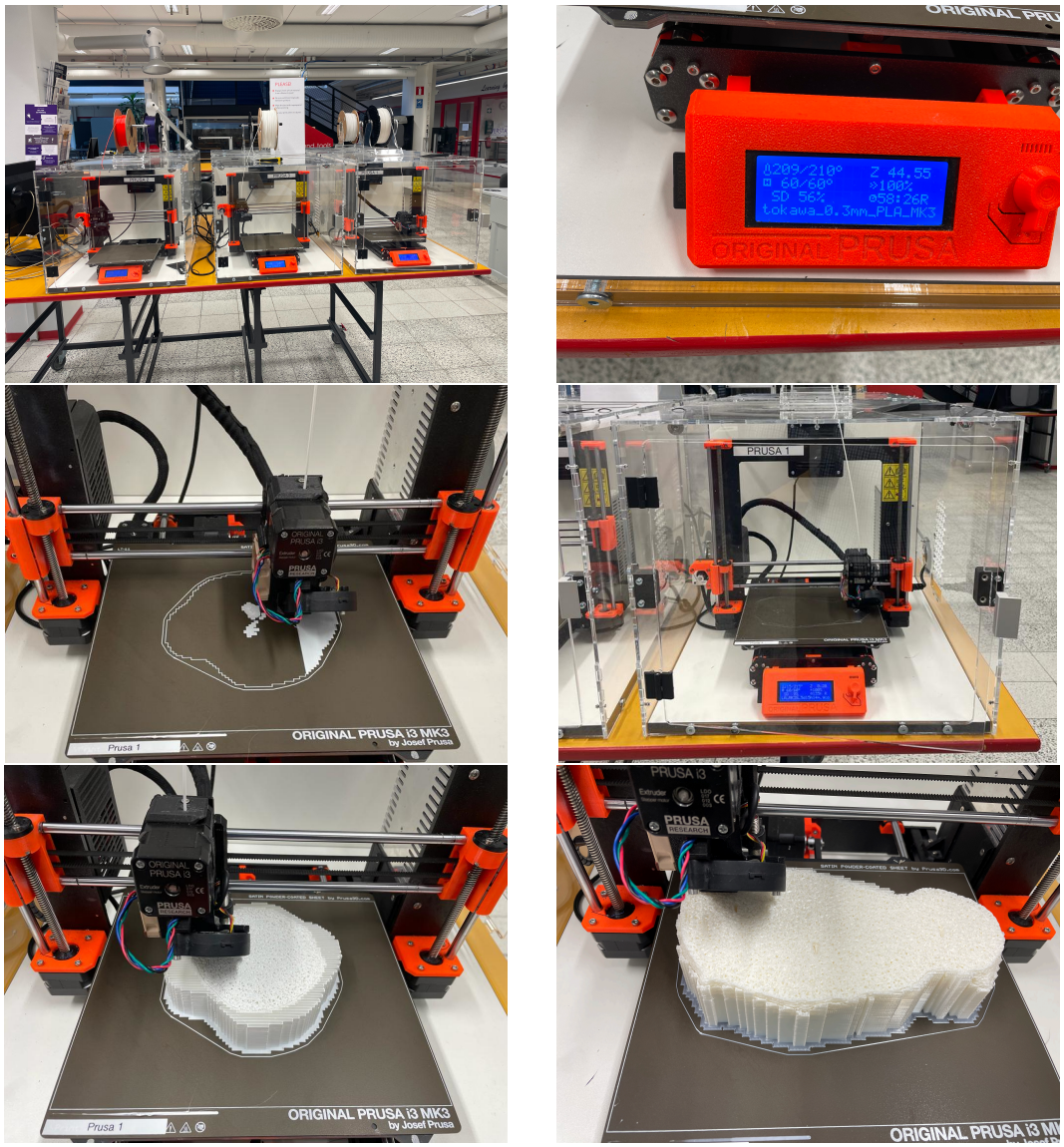

Figure 6.3 *This figure shows images from the experimental printing process of the Itokawa model using PLA at Fablab in Tampere University in August 2022.*

Printing Process of the Itokawa Model

At approximately 56% of the printing process of the Itokawa model, an image is taken of the procedure, at this point we witness the three separate fractures built into the model. At the 72% printing mark, the layers are also apparent, as we can see. Finally, the Itokawa asteroid model assumes the form of the Itokawa asteroid and displays rough surfaces. Thus showing that the entire process was successful, from conception to execution.

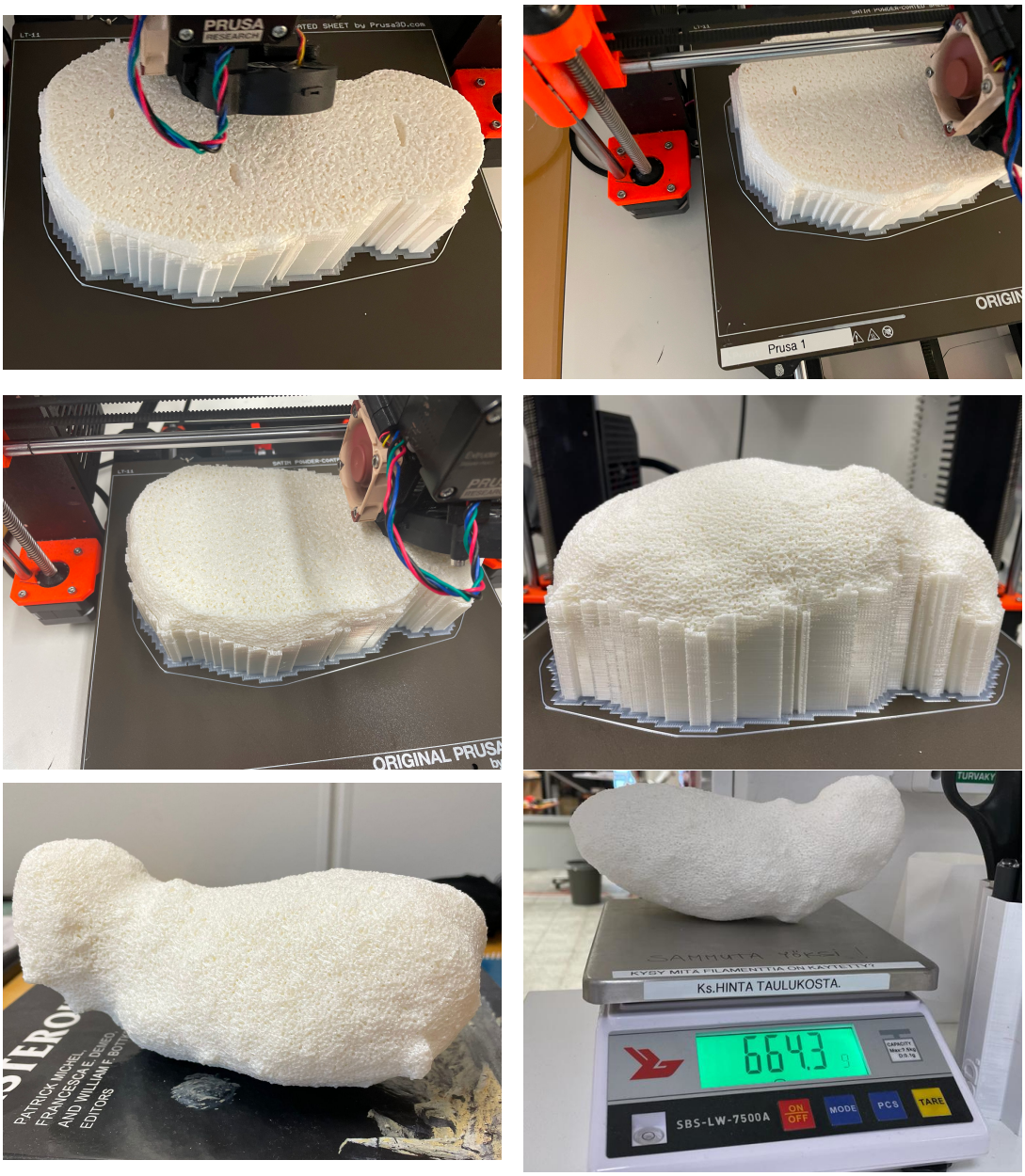

Figure 6.4 *This figure visualises images of the Itokawa model showing various fractures and layers at different printing times, using the experimental material PLA.*

6.3.2 Final Printing Process

Generally, printing with ABS is more complicated than printing with PLA, and so we printed several attempts in the lab in order to arrive at a successful model, however, there were a couple of failed prints which had cracks and layer incoherence. On the first trial, the nozzle temperature of 270°C was too high, and while the model appeared to be printing fine at first, it began to have slight surface cracks around the 68% mark. The model printed fine on the second trial with a slightly lower nozzle temperature until it was necessary to substitute the filament row with a new

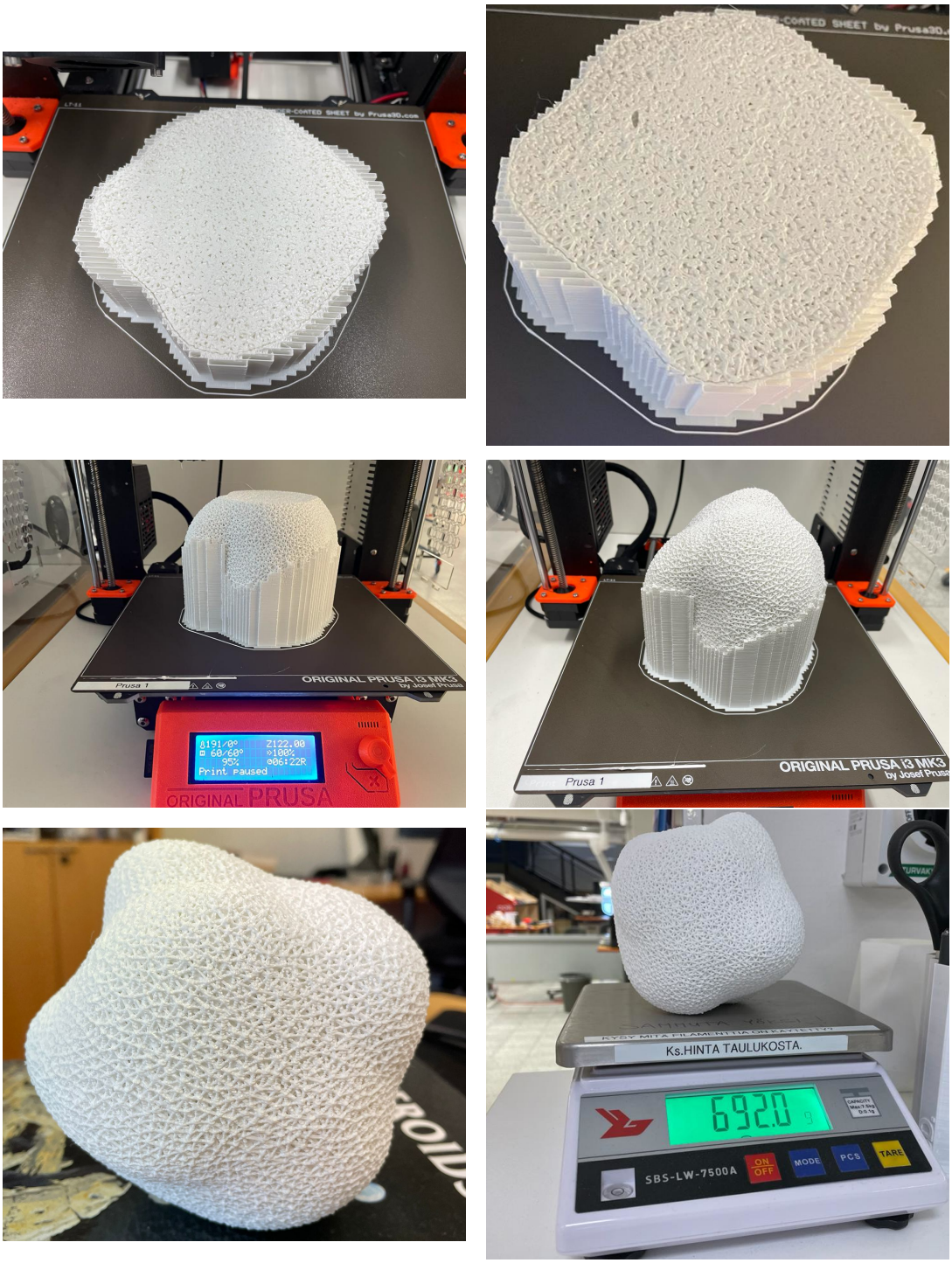

Figure 6.5 *This figure shows images of the KY model showing various fractures and layers which was printed experimentally with PLA.*

one, which caused a layer shift and thus a failed print. Figures 6.7 show visual representations of these two scenarios. However, we then decided to print the models in parallel on two separate Prusa i3 MK3S+ printers using the ABS650 filament on one and the ABS450 on another. By learning from previous trials we discovered that it was best to print the model at around 245°C which helped

to avoid warping of the model and thus cracks. Layer shifts were also prevented by employing a filament feeder (Pallete 2), which automatically supplied many filaments into the printer without the need for human filament row changes. Additionally, the draft shield was activated, adding additional covering surrounding the model and aiding in heat retention to prevent warping. To get the best print possible of the Itokawa model, it was also essential to reduce the printing speed to approximately 70% . The ABS450 filament produced a successful print while the ABS650 filament jammed during the printing process. It is clear that the ABS650 is a significantly more complex filament, and printing such sophisticated models on a conventional printer using this filament may not be possible. Figure 6.8 shows different views of the final successful print of the Itokawa Model while Figure 6.6 shows all successfully printed models together.

Figure 6.6 *This figure shows all the bunny, spheres (3 printed with ABS450, 3 printed with ABS650), KY and Itokawa (2 printed PLA and ABS450) models together that were successfully printed at Fablab Tampere.*

Figure 6.7 *This figure shows images of the failed printing process of the Itokawa model which have defects such as cracks and layer incoherence caused by layer shifts and high temperatures and warping. The ABS650 filament was used in printing this model.*

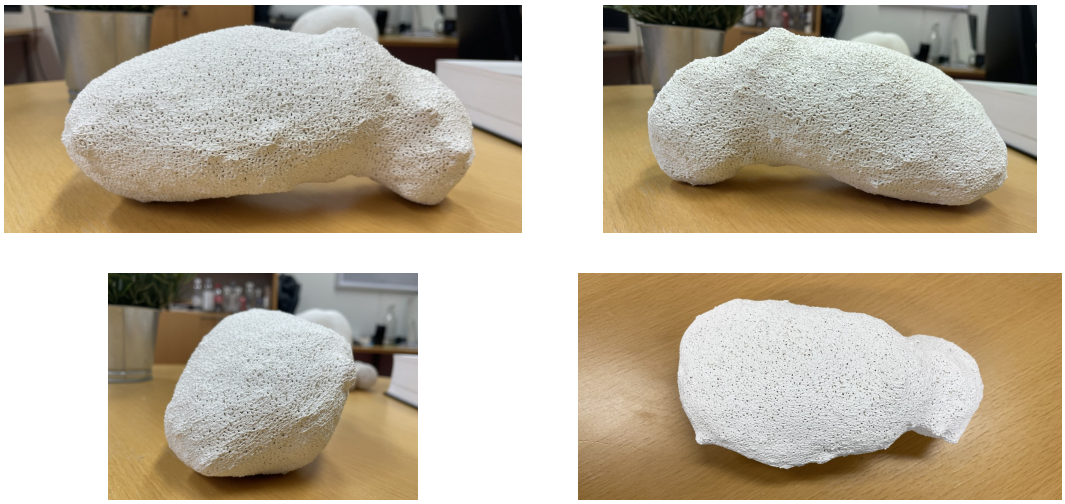

Figure 6.8 *This figure shows different views of the final optimal model of the asteroid Itokawa printed using ABS450 filament printed at Fablab Tampere.*

SPECIFICATIONS	ITOKAWA	KY
Weight	664.3 grams	692.1 grams
Print time	6 Days	6 Days
Filament	PLA	PLA
Printer Type	PRUSA i3 MK3+	PRUSA i3 MK3+
Nozzle Temperature	245-250 °C	245-250 °C
Plate Temperature	110-112 °C	110-112 °C

Table 6.2 *Settings used on the Pruserslicer software ranging from temperature parameters to the nozzle sizes as well as the density for printing the asteroid models.*

6.3.3 Time of Computation

The model's computation, including the use of the wireframe function to interpolate the finite element mesh used approximately 16GB of RAM and took around 12 minutes. The printing of both the experimental and final models took approximately 6 days for trial prints and 7 days for the final print.

7 Conclusion

Scientists have demonstrated that the course of an asteroid can be slightly shifted and thus alter its orbit through the success of the recently completed Dart Mission (Cheng et al. 2012; NASA 2022a). This is a significant step forward for planetary defence, but it is only the tip of the iceberg when thinking about what can be accomplished. The total cost of the DART mission is estimated to be around 324.5 million USD (Parsons 2021), which is a substantial amount of money. As a result, developing asteroid models that depict ideal asteroid properties and can aid in lab simulations and other forms of analysis on Earth is critical, as this would help to reduce costs and margins for error in future space missions.

This thesis aimed to create an analogue with a predetermined permittivity structure that can be utilized to computationally find fractures inside the complex 3D model of the asteroid Itokawa. Through a more in-depth analysis, this thesis further extended the research carried out by Sorsa et al. 2021b which says that fused filament fabrication can be used to produce an asteroid analogue object as well as the findings by Eyraud et al. 2020 and Sorsa et al. 2021a which show that an analogue can be reconstructed with an ellipsoid inside. We created fractures with diameters less than $\lambda/2$ in one direction, making them nearly unidentifiable in a linear radar reconstruction. As a result, we have improved the coherence of the filling levels and permittivity, which can be used to print a 3D asteroid model successfully.

This thesis consisted of a methodological and an experimental part, the Itokawa model's dielectric properties were developed using the Maxwell Garnett formula (Sihvola et al. 1985), which has proven to be reliable in space research. Additionally, because it provided a stable dielectric constant with low losses over a wide frequency and temperature range, the ABS450 (PREMIX 2019) designed for extrusion was chosen as the best material for printing the 3D model using a traditional 3D printer. Using MATLAB, we created a 3D printable prismatic surface mesh from a given tetrahedral by refining the meshes and substituting the edges of the meshes with overlapping regular prisms. We tested the model's accuracy in a variety of ways, including analyzing its numerical and experimental accuracy, as well as comparing it to experimental objects (spheres, bunny).

The results demonstrated that the ideal permittivity of a complex asteroid model could be controlled and thus 3D printed using materials such as ABS450 (PREMIX 2019). Table 6.2 discussed the best 3D printer settings for an ideal print of the asteroid model. The results also showed that different layers, edges, and fractures could be incorporated by adjusting the model's

edge width and volumetric filling relationships and that when both edge threshold and correction were applied, we obtained the best result that was closest to the referential data.

Future research on this topic will also include developing the model further with a focus on the cracks/fractures to better understand what is inside an asteroid, giving the ability to control not only the model's permittivity but also the shapes in the interior. Additionally, the task's complexity made it difficult to convince a business to commit to printing the models as a sub-contracted task. However, by incorporating an industrial printer, which could be faster and less error-prone than the PRUSA i3 MK3+ used in this research, the efficiency of the process can be further increased. All of this put together would be very beneficial to space research especially future space missions.

The source code for the wireframe function in this thesis is included in Appendix A. The same method can be applied in fields such as biomedical engineering and biotechnology, which use computer radar tomography to scan human beings.

Bibliography

Alfvén, H. (1982). "The origin of the Solar System". In: *Evolution in the Universe*, p. 31.

Asphaug, E, M. Belton, and R. Kakuda (2001). "Geophysical exploration of asteroids: the Deep interior mission concept". In: *Lunar and Planetary Science Conference*, p. 1867.

Barnouin-Jha, O. S. et al. (2008). "Small-scale topography of 25143 Itokawa from the Hayabusa laser altimeter". In: *Icarus* 198.1, pp. 108–124.

Berry, K. et al. (2013). "OSIRIS-REx touch-and-go (TAG) mission design and analysis". In: *36th Annual AAS Guidance and Control Conference*. GSFC. CP. 7566.2013.

Bottke, W. F., F. E. DeMeo, and P. Michel (2015). *Asteroids IV*. University of Arizona Press.

Bottke Jr, W. F. et al. (2002). "An overview of the asteroids: the asteroids III perspective". In: *Asteroids III* 1, pp. 3–15.

Catapano, I. et al. (2011). "A tomographic approach for helicopter-borne ground penetrating radar imaging". In: *IEEE Geoscience and Remote Sensing Letters* 9.3, pp. 378–382.

Cheng, A. et al. (2012). "Dart: Double asteroid redirection test". In: *European Planetary Science Congress*. Vol. 7, pp. 23–28.

Cheng, A. F. et al. (2018). "AIDA DART asteroid deflection test: Planetary defense and science objectives". In: *Planetary and Space Science* 157, pp. 104–115.

Colin, L. (1980). "The pioneer Venus program". In: *Journal of Geophysical Research: Space Physics* 85.A13, pp. 7575–7598.

Dionisio, J. D. N., W. G. B. III, and R. Gilbert (2013). "3D virtual worlds and the metaverse: Current status and future possibilities". In: *ACM Computing Surveys (CSUR)* 45.3, pp. 1–38.

Erasmus, N et al. (2017). "Characterization of near-earth asteroids using KMTNET-SAAO". In: *The Astronomical Journal* 154.4, p. 162.

Eyraud, C. et al. (2020). "Full wavefield simulation versus measurement of microwave scattering by a complex 3D-printed asteroid analogue". In: *Astronomy & Astrophysics* 643, A68.

Fujiwara, A. et al. (2006). "The rubble-pile asteroid Itokawa as observed by Hayabusa". In: *Science* 312.5778, pp. 1330–1334.

Glassmeier, K.-H. et al. (2007). "The Rosetta mission: flying towards the origin of the solar system". In: *Space Science Reviews* 128.1, pp. 1–21.

Haruyama, J et al. (2017). "Detection of lunar lava tubes by lunar radar sounder onboard selene (kaguya)". In: *48th Annual Lunar and Planetary Science Conference*. 1964, p. 1711.

Hestroffer, D. et al. (2019). "Small solar system bodies as granular media". In: *The Astronomy and Astrophysics Review* 27.1, pp. 1–64.

Ivanovich, G. S. and G. S. Ivanovich (2008). *Salyut: The First Space Station: Triumph and Tragedy*. Springer.

JAXA (2003). *Close-Up on the Asteroid Itokawa*. URL: https://global.jaxa.jp/article/special/hayabusa_sp3/index_e.html (visited on 01/17/2022).

Jol, H. M. (2008). *Ground penetrating radar theory and applications*. elsevier.

Jones, G. (2022). *Introduction to PrusaSlicer*. URL: www.ucl.ac.uk/mssl/research/solar-system/planetary-science/what-planetary-science (visited on 02/28/2022).

Kofman, W. et al. (2007). "The Comet Nucleus Sounding Experiment by Radiowave Transmission (CONSERT): A short description of the instrument and of the commissioning stages". In: *Space Science Reviews* 128.1, pp. 413–432.

Kofman, W. et al. (2015). "Properties of the 67P/Churyumov-Gerasimenko interior revealed by CONSERT radar". In: *Science* 349.6247, aab0639.

Kuninaka, H. (2020). "Hayabusa and Hayabusa2 asteroid sample return missions and the beyond". In: *Advances in Optical and Mechanical Technologies for Telescopes and Instrumentation IV*. Vol. 11451. SPIE, p. 1145103.

Lauretta, D. et al. (2017). "OSIRIS-REx: sample return from asteroid (101955) Bennu". In: *Space Science Reviews* 212.1, pp. 925–984.

Li, C. et al. (2020). "The Moon's farside shallow subsurface structure unveiled by Chang'E-4 Lunar Penetrating Radar". In: *Science advances* 6.9, eaay6898.

Lintott, C. et al. (2011). "Galaxy Zoo 1: data release of morphological classifications for nearly 900 000 galaxies". In: *Monthly Notices of the Royal Astronomical Society* 410.1, pp. 166–178.

McDaid, L. (2006). "Pluto downgraded". In: *Skeptic (Altadena, CA)* 13.1, pp. 9–10.

NASA (2022a). *DART's Final Images Prior to Impact*. URL: https://www.nasa.gov/feature/dart-s-final-images-prior-to-impact (visited on 09/27/2022).

— (2022b). *Solar System Overview*. URL: https://solarsystem.nasa.gov/solar-system/beyond/overview/ (visited on 02/26/2022).

O'Leary, B. (1999). *The new solar system*. Cambridge University Press.

Parsons, J. (2021). *NASA and SpaceX to crash satellite into an asteroid - here's why*. URL: https://metro.co.uk/2021/11/22/nasa-dart-mission-cost-location-and-how-it-stops-an-asteroid-impact-15643435/ (visited on 11/06/2022).

Persico, A. R. et al. (2018). "Cubesat-based passive bistatic radar for space situational awareness: A feasibility study". In: *IEEE Transactions on Aerospace and Electronic Systems* 55.1, pp. 476–485.

Porcello, L. J. et al. (1974). "The Apollo lunar sounder radar system". In: *Proceedings of the IEEE* 62.6, pp. 769–783.

PREMIX (2019). *Preperm ABS650 Technical Data sheet*. URL: https://www.preperm.com/webshop/wp-content/uploads/2018/04/PREPERM_ABS650_TDS.pdf (visited on 04/26/2022).

Prusa, J. (2022). *What is Planetary Science*. URL: www.prusa3d.com/page/prusaslicer_424/ (visited on 04/14/2022).

Pursiainen, S. and M. Kaasalainen (2016). "Orbiter-to-orbiter tomography: a potential approach for small solar system bodies". In: *IEEE Transactions on Aerospace and Electronic Systems* 52.6, pp. 2747–2759. DOI: 10.1109/TAES.2016.150638.

Pursiainen, S. et al. (May 2020). *Asteroid Wireframe Package*. Version 1.0. This research was supported by the Academy of Finland Centre of Excellence in Inverse Modelling and Imaging 2018-2025 and Centre Commun de Ressources en Microondes. DOI: 10.5281/zenodo.3838480. URL: https://doi.org/10.5281/zenodo.3838480.

Reich, E. S. (2010). "NASA panel weighs asteroid danger: telescopes in space could help pin down the risk of a deadly impact". In: *Nature* 467.7312, pp. 140–142.

Rossi, B. (2015). *Data revolution: the gold rush of the 21st century*. URL: https://www.information-age.com/data-revolution-gold-rush-21st-century-2-123460039/ (visited on 11/03/2022).

Saito, J et al. (July 2006). "Detailed Images of Asteroid 25143 Itokawa from Hayabusa". In: *Science (New York, N.Y.)* 312, pp. 1341–4. DOI: 10.1126/science.1125722.

Sears, D. et al. (2004). "The Hera mission: multiple near-earth asteroid sample return". In: *Advances in space research* 34.11, pp. 2270–2275.

Sihvola, A., E. Nyfors, and M. Tiuri (1985). "Mixing formulae and experimental results for the dielectric constant of snow". In: *Journal of Glaciology* 31.108, pp. 163–170.

Sinelnikov, V., V. Kuznetsov, and S. Alpert (2014). "Sputnik 1 and the first satellite ionospheric experiment". In: *40th COSPAR Scientific Assembly* 40, pp. C0–2.

Sorsa, L.-I. (2018). "Realistic asteroid interior models and full-wave tomography simulation". MA thesis.

— (2021). "Full-Wave Radar Tomography of Complex, High-Contrast Targets: Imaging the Interior Structure of a Small Solar System Body". PhD thesis.

Sorsa, L.-I., S. Pursiainen, and C. Eyraud (2021a). "Analysis of full microwave propagation and backpropagation for a complex asteroid analogue via single-point quasi-monostatic data". In: *Astronomy & Astrophysics* 645, A73.

Sorsa, L.-I. et al. (2019). "Bistatic full-wave radar tomography detects deep interior voids, cracks, and boulders in a rubble-pile asteroid model". In: *The Astrophysical Journal* 872.1, p. 44.

Sorsa, L.-I. et al. (2021b). “Complex-structured 3D-printed wireframes as asteroid analogues for tomographic microwave radar measurements”. In: *Materials & Design* 198, p. 109364.

Suzy, S. (2022). *Asteroid Belt Facts*. URL: `https://theplanets.org/asteroid-belt/` (visited on 02/26/2022).

Talbert, T. (2021). *NASA Crashing a Spacecraft into an Asteroid*. URL: `www.nasa.gov/feature/episode-15-we-asked-a-nasa-scientist-is-nasa-really-crashing-a-spacecraft-into-an-asteroid` (visited on 01/17/2022).

Times, N. Y. (2021). *Facebook Renames Itself Meta*. URL: `https://www.nytimes.com/2021/10/28/technology/facebook-meta-name-change.html` (visited on 10/28/2021).

Trust, T. and R. W. Maloy (2017). “Why 3D print? The 21st-century skills students develop while engaging in 3D printing projects”. In: *Computers in the Schools* 34.4, pp. 253–266.

Wang, R et al. (2020). “Topographic Mapping and Analysis based on 3D Reconstruction Model of Simulated Asteroid.” In: *International Archives of the Photogrammetry, Remote Sensing & Spatial Information Sciences* 43.

West, D. (2022). “Neil Armstrong: Astronaut and the First Man to Walk on the Moon”. In: *Humanities*.

Yusuf, Y. O. et al. (2021). “Investigation of Phase and Wavelength-induced Errors in Full-Wave Radar Tomography of High Contrast Domain: an Application to Small Solar System Bodies”. In: *arXiv preprint arXiv:2110.05106*.

— (2022). “Investigation of wavelength-induced uncertainties in full-wave radar tomography of high contrast domain: An application to small solar system bodies”. In: *Icarus* 387, p. 115173.

Appendices

A Wireframe Function

```
function [m_triangles,m_nodes,filling_vec,w_vec,shape_vec] = ...
wireframe(tetra,nodes,filling_vec,varargin)
%This is a wireframe function to create a prismatic surface mesh out
%of a given volumetric %tetrahedral mesh for 3D printing purpose.
%Inputs: tetra (N-by-4 array) containing the tetrahedra of the mesh,
%nodes (M-by-3 array)
%Outputs:

%*********************************************************************
%Initialization part to set the parameters.
%*********************************************************************

R = 4/3*pi*(0.5)^3;
overlap_param = R^(1/3)/2;
printer_buffer = sqrt(3);
printer_resolution = 0;
n_mesh_refinement = 0;
edge_threshold = 0;
scaling_constant = 1;
n_iter = 10000;
filling_vec = filling_vec(:);

if length(filling_vec) == 1
    filling_vec = filling_vec*ones(size(tetra,1),1);
elseif length(filling_vec) < size(tetra,1)
    domain_ind_vec = unique(tetra(:,5));
    filling_vec_aux = zeros(size(tetra,1),1);
for i = 1 : length(domain_ind_vec)
    I = find(tetrahedra(:,5)==domain_ind_vec(i));
    filling_vec_aux(I) = filling_vec(i);
end
    filling_vec = filling_vec_aux;
end


if not(isempty(varargin))
    printer_resolution = varargin{1};
```

```
if length(varargin) > 1
    n_mesh_refinement = varargin{2};
end
if length(varargin) > 2
    scaling_constant = varargin{3};
    nodes = scaling_constant*nodes;
end
if length(varargin) > 3
    edge_threshold = varargin{4};
end
end

%%%%%%%%%%%%%%%%%%%%%%%%%%%%%%%%%%%%%%%%%%%%%%%%%%%%%%%%%%%%%%%%%%%%%%%%
%Mesh refinement, if requested
%%%%%%%%%%%%%%%%%%%%%%%%%%%%%%%%%%%%%%%%%%%%%%%%%%%%%%%%%%%%%%%%%%%%%%%%

if n_mesh_refinement > 0
    domain_ind = tetra(:,5);
for i = 1 : n_mesh_refinement
  [nodes,tetra,interp_vec] = refine_mesh(nodes,tetra);
  domain_ind = domain_ind(interp_vec);
  filling_vec = filling_vec(interp_vec);
end
tetra = [tetra domain_ind];
end

%%%%%%%%%%%%%%%%%%%%%%%%%%%%%%%%%%%%%%%%%%%%%%%%%%%%%%%%%%%%%%%%%%%%%%%%
%Prism creation.
%%%%%%%%%%%%%%%%%%%%%%%%%%%%%%%%%%%%%%%%%%%%%%%%%%%%%%%%%%%%%%%%%%%%%%%%

n_nodes = size(nodes,1);
n_tetra = size(tetra,1);

Aux_mat = [nodes(tetra(:,1),:)'; nodes(tetra(:,2),:)'; ...
           nodes(tetra(:,3),:)'] - repmat(nodes(tetra(:,4),:)',3,1);
ind_m = [1 4 7; 2 5 8 ; 3 6 9];
volume = abs(Aux_mat(ind_m(1,1),:).*(Aux_mat(ind_m(2,2),:).*Aux_mat(ind_m(3,3),:) ...
-Aux_mat(ind_m(2,3),:).*Aux_mat(ind_m(3,2),:)) ...
 - Aux_mat(ind_m(1,2),:).*(Aux_mat(ind_m(2,1),:).*Aux_mat(ind_m(3,3),:) ...
-Aux_mat(ind_m(2,3),:).*Aux_mat(ind_m(3,1),:)) ...
+ Aux_mat(ind_m(1,3),:).*(Aux_mat(ind_m(2,1),:).*Aux_mat(ind_m(3,2),:) ...
-Aux_mat(ind_m(2,2),:).*Aux_mat(ind_m(3,1),:)))/6;
```

```
p_triangles = [
     4     2     1
     2     6     1
     3     4     1
     1     5     3
     1     6     5
     4     6     2
     3     6     4
     3     5     6
     ];

 ind_m = [
           1 2 ;
           1 3 ;
           1 4 ;
           2 3 ;
           2 4 ;
           3 4
           ];

tetra_sort = [
              tetra(:,[1 2]) ones(size(tetra,1),1) [1:size(tetra,1)]' tetra(:,5) ... tetra(:,[3 4]);
              tetra(:,[1 3]) 2*ones(size(tetra,1),1) [1:size(tetra,1)]' ...
              tetra(:,5) tetra(:,[2 4]);
              tetra(:,[1 4]) 3*ones(size(tetra,1),1) [1:size(tetra,1)]' ...
              tetra(:,5) tetra(:,[2 3]);
              tetra(:,[2 3]) 4*ones(size(tetra,1),1) [1:size(tetra,1)]' ...
              tetra(:,5) tetra(:,[1 4]);
              tetra(:,[2 4]) 5*ones(size(tetra,1),1) [1:size(tetra,1)]' ...
              tetra(:,5) tetra(:,[1 3]);
              tetra(:,[3 4]) 6*ones(size(tetra,1),1) [1:size(tetra,1)]' ...
              tetra(:,5) tetra(:,[1 2]);
              ];

tetra_sort(:,1:2) = sort(tetra_sort(:,1:2),2);
tetra_sort = sortrows(tetra_sort,[1 2]);
tetra_ind = zeros(size(tetra_sort,1),1);
[u_aux, u_ind, u_ind_orig] = unique(tetra_sort(:,1:2),'rows');
tetra_ind = sub2ind(size(tetra),repmat(tetra_sort(u_ind,4),1,2),...
ind_m(tetra_sort(u_ind,3),:));
edges = [tetra(tetra_ind) tetra_sort(u_ind,3) tetra_sort(u_ind,4) ...
tetra_sort(u_ind,5)];
n_edges = size(edges,1);
```

```
%*********************************************************************
%Matrix construction for finding the edge-widths by iteration.
%*********************************************************************

c_ind = unique(tetra(:,5));

d_edges = nodes(edges(:,2),:) - nodes(edges(:,1),:);

E_mat_0 = sparse(tetra_sort(:,6),u_ind_orig,ones(size(tetra_sort(:,6))), ...
n_nodes,n_edges);
E_mat_0 = E_mat_0 + sparse(tetra_sort(:,7),u_ind_orig,...
ones(size(tetra_sort(:,7))), n_nodes,n_edges);
[I,J] = find(E_mat_0==1);
f_vec_aux = ones(n_edges,1);
f_vec_aux(J) = 2;

E_mat_2 = sparse(tetra_sort(:,4),u_ind_orig,volume(tetra_sort(:,4)),...
n_tetra,n_edges);
e_vec_aux = full(sum(E_mat_2))';
e_vec_aux = e_vec_aux.*f_vec_aux;

V_mat_aux_1 = sparse(u_ind_orig,tetra_sort(:,1),ones(size(u_ind_orig,1),1),...
n_edges,n_nodes);
v_vec_aux_1 = full(sum(V_mat_aux_1))';
clear V_mat_aux_1;

V_mat_aux_2 = sparse(u_ind_orig,tetra_sort(:,2),ones(size(u_ind_orig,1),1),...
n_edges,n_nodes);
v_vec_aux_2 = full(sum(V_mat_aux_2))';
clear V_mat_aux_2;

E_mat_1 = sparse(tetra_sort(:,4),u_ind_orig,volume(tetra_sort(:,4))'.*...
(sqrt(3)/4).*sqrt(sum(d_edges(u_ind_orig,:).^2,2))./e_vec_aux(u_ind_orig),...
n_tetra,n_edges);
E_mat_2 = sparse(tetra_sort(:,4),u_ind_orig,volume(tetra_sort(:,4))'./...
((sqrt(3)/4).*sqrt(sum(d_edges(u_ind_orig,:).^2,2)).*e_vec_aux(u_ind_orig)),...
n_tetra,n_edges);
E_mat_3 = sparse(tetra_sort(:,4),u_ind_orig,volume(tetra_sort(:,4))'.*2.*...
overlap_param.*(sqrt(3)/4)./(e_vec_aux(u_ind_orig)),n_tetra,n_edges);
E_mat_4 = sparse(tetra_sort(:,4),u_ind_orig,volume(tetra_sort(:,4))'.*2.*...
overlap_param.*(sqrt(3)/4).*(1./v_vec_aux_1(tetra_sort(:,1)) + 1./v_vec_aux_2(tetra_sort(:,2)))./...
(e_vec_aux(u_ind_orig)),n_tetra,n_edges);
```

```
D_mat = spdiags(volume',0,n_tetra,n_tetra);
D_mat_inv = spdiags(1./volume',0,n_tetra,n_tetra);

%w_vec = E_mat_2'*D_mat*filling_vec;
w_vec = zeros(size(E_mat_2,2),1);

reg_param = 1;
i = 0;
norm_val = norm(filling_vec - D_mat_inv*E_mat_2*w_vec)/norm(filling_vec);
while norm_val >= 0.01 && i < n_iter
    i = i + 1;
    w_vec = w_vec + reg_param*E_mat_2'*(filling_vec - D_mat_inv*E_mat_2*w_vec);
    w_vec = max(0,w_vec);
    norm_val = norm(filling_vec - D_mat_inv*E_mat_2*w_vec)/norm(D_mat*filling_vec)
end

%*********************************************************************
%Iteration to find the edge-widths given the filling ratio
%*********************************************************************

i = 0;
w_vec_old = zeros(size(w_vec));
while norm(w_vec - w_vec_old)/norm(w_vec) > 1e-8 && i < n_iter
i = i + 1;
w_vec_old = w_vec;
w_vec = sum(filling_vec)*w_vec./sum(D_mat_inv*(E_mat_1*w_vec - E_mat_3*...
(w_vec).^(3/2) + E_mat_4*(w_vec).^(3/2)));
I = intersect(find(sqrt(w_vec) >= edge_threshold/2),find(sqrt(w_vec) ...
< edge_threshold));
w_vec(I) = edge_threshold.^2;
I = find(sqrt(w_vec) < edge_threshold);
w_vec(I) = 0;
end

filling_vec = D_mat_inv*(E_mat_1*w_vec - E_mat_3*(w_vec).^(3/2) +...
E_mat_4*(w_vec).^(3/2));
filling_vec = min(filling_vec,1);

w_vec = sqrt(w_vec + printer_buffer*printer_resolution.^2);

shape_vec = w_vec./sqrt(sum(d_edges.^2,2));
```

```
I = setdiff([1:size(w_vec,1)]',I);
w_vec = w_vec(I);
shape_vec = shape_vec(I);
edges = edges(I,:);

m_triangles = zeros(8*size(edges,1),3);
m_nodes = zeros(6*size(edges,1),3);

%*********************************************************************
%Edge-extension to set the overlap of the edges.
%*********************************************************************

for j = 1 : size(edges,1)

    p_nodes = [
   -0.5774          0-shape_vec(j)*overlap_param           0
   -0.5774     1.0000+shape_vec(j)*overlap_param           0
    0.2887           0-shape_vec(j)*overlap_param     -0.5000
    0.2887     1.0000+shape_vec(j)*overlap_param     -0.5000
    0.2887           0-shape_vec(j)*overlap_param      0.5000
    0.2887     1.0000+shape_vec(j)*overlap_param      0.5000
    ];

d_edge = nodes(edges(j,2),:) - nodes(edges(j,1),:);
edge_length = sqrt(sum(d_edge.^2,2));
d_edge = d_edge/edge_length;
[m_val,m_ind] = max(abs(d_edge));
n_ind = find(not(ismember([1 2 3],m_ind)));
d_cross_1(n_ind(1)) = d_edge(n_ind(2));
d_cross_1(n_ind(2)) = d_edge(n_ind(1));
d_cross_1(m_ind) = -2*d_edge(n_ind(1))*d_edge(n_ind(2))/d_edge(m_ind);
d_cross_1 = d_cross_1/sqrt(sum(d_cross_1.^2,2));
d_cross_2 = cross(d_cross_1', d_edge')';

m_triangles((j-1)*8+1:j*8,:) = p_triangles + (j-1)*6;
m_nodes((j-1)*6+1:j*6,:) = p_nodes*edge_length*[shape_vec(j)*d_cross_1 ; d_edge;  shape_vec(j)*d_cross_2] +
end

m_triangles = m_triangles(:,[1 3 2]);
end

%*********************************************************************
```

```
function [nodes,tetra,interp_vec] = refine_mesh(nodes,tetra)

%*********************************************************************
%Refinement function.
%*********************************************************************

tetra_sort = [tetra(:,[1 2]);
              tetra(:,[2 3]);
              tetra(:,[3 1]);
              tetra(:,[1 4]);
              tetra(:,[2 4]);
              tetra(:,[3 4]);
              ];

tetra_sort = sort(tetra_sort,2);
[edges,edges_ind_1,edges_ind_2] = unique(tetra_sort,'rows');
edges_ind = reshape(edges_ind_2,size(edges_ind_2,1)/6,6);

edges_ind = edges_ind + size(nodes,1);
nodes = [nodes ; 0.5*(nodes(edges(:,1),:) + nodes(edges(:,2),:))];

interp_vec = repmat([1:size(tetra,1)]',8,1);

tetra  = [tetra(:,1) edges_ind(:,1) edges_ind(:,3) edges_ind(:,4)  ;
                     edges_ind(:,1)  tetra(:,2) edges_ind(:,2) ...
                     edges_ind(:,5)  ;
                      edges_ind(:,3) edges_ind(:,2) tetra(:,3) ...
                      edges_ind(:,6) ;
                      edges_ind(:,4) edges_ind(:,5) edges_ind(:,6) ...
                      tetra(:,4) ;
                       edges_ind(:,3) edges_ind(:,4) edges_ind(:,1)...
                       edges_ind(:,6) ;
                       edges_ind(:,6) edges_ind(:,5) edges_ind(:,1) ...
                       edges_ind(:,2) ;
                       edges_ind(:,4) edges_ind(:,1) edges_ind(:,6) ...
                       edges_ind(:,5) ;
                       edges_ind(:,3) edges_ind(:,1) edges_ind(:,2) ...
                       edges_ind(:,6)
                       ];


end
```